Dissertation for Doctoral Degree of Engineering

Functional Layer-by-Layer Engineering for Advanced Organic Field-Effect Transistors and Light-Emitting Transistors

고성능 유기 전계 효과 트랜지스터 및
유기 발광 트랜지스터를 위한
단계적 기능층 공정 연구

by

Chang-Min Keum

August 2014

Department of Electrical Engineering and Computer Science
College of Engineering
Seoul National University

Functional Layer-by-Layer Engineering for Advanced Organic Field-Effect Transistors and Light-Emitting Transistors

지도교수 이 신 두

이 논문을 공학박사 학위논문으로 제출함

2014 년 8 월

서울대학교 대학원

공과대학 전기·컴퓨터공학부

금 창 민

금 창 민 의 박사 학위논문을 인준함

2014 년 6 월

위 원 장 이 창 희 (인)

부위원장 이 신 두 (인)

위 원 최 종 선 (인)

위 원 배 진 혁 (인)

위 원 김 민 회 (인)

Abstract

Functional Layer-by-Layer Engineering for Advanced Organic Field-Effect Transistors and Light-Emitting Transistors

Chang-Min Keum

Department of Electrical and Computer Engineering

The Graduate School

Seoul National University

Recent progress in the electrical performance and physical understanding of both organic materials and devices has led to the advent of a new era of organic electronics including flexible and large-area electronics, low-cost printed electronics, and optoelectronics. The intrinsic advantages of organic semiconductors such as the flexibility in design and the versatile processing capability provide a broad range of strategies for manipulating functional materials and fabricating advanced organic electronic devices. As one of the representative of them, organic field-effect transistors (OFETs) are expected to serve as key elements for practical applications in flexible displays, radio-frequency identification tags, and sensors.

Among the numerous issues regarding the OFETs, different types of solution-processes applicable for flexible, large-area, and low-cost organic electronics have been extensively investigated owing to the capability of low temperature processing and the simplicity in fabrication by versatile printing methods, for example, roll-to-roll processing, and inkjet printing. Since the solution-process basically involves spreading and drying of a liquid on a solid surface, key ingredients are the engineering of the solid/liquid interfaces and the understanding of the thermodynamic behavior of the liquid state. Another issue is on the functionality of the OFET for sophisticated electronic and optoelectronic systems. For example, organic light-emitting transistors (OLETs) possess the light-emitting capability together with the electrical switching property of the transistors so that they have great potential for use as future displays. Despite such advantages as the electroluminescence quantum efficiency and the aperture ratio beyond organic light-emitting diodes, however, typical OLETs suffer from the intrinsic line emission characteristics which allow only limited applications.

This thesis primarily aims to demonstrate functional layer-by-layer engineering approaches to the development of advanced OFETs and OLETs, and deals with two major categories, one of which concerns the solution-processed OFETs and the other vertical OLETs (VOLETs) showing the quasi-surface emission.

Firstly, a solution-processed OFET with low leakage current and self-pattern registration is demonstrated using a patterned dielectric barrier (PDB). The PDB of a hydrophobic fluoro-polymer enables to effectively reduce the

vertical charge flow generated from the gate electrode and to spontaneously define an active channel pattern by means of the selective wettability together with the geometrical confinement. Next, two viable methods of inducing the molecular order of solution-processed organic semiconductors and the resultant mobility enhancement are described. Since the molecular ordering of an organic semiconductor strongly depends on the spreading and drying processes, the dynamic control of the two processes plays a critical role in the electrical performance of a solution-processed organic device. A temperature gradient-assisted anisotropic solvent drying method and a new approach to the unidirectional topography of an inkjet-printed polymer insulator are developed to control the spreading and drying processes of the solution.

Secondly, the VOLET with a network electrode of closed topology for quasi-surface emission is developed. Due to the closed topology in the network of the source electrode, the charge transport and the resultant carrier recombination are substantially extended from individual network boundaries toward the corresponding aperture centers in the source electrode. The spatial distribution of the surface emission depends primarily on the relative scale of the aperture in the network electrode to the characteristic length for the charge carrier recombination. For characterizing the apparent carrier recombination zone for light emission on a macroscopic level, an optical methodology is newly introduced.

In summary, the functional layer-by-layer engineering and novel device architectures are investigated toward the development of advanced organic electronics and optoelectronics within the framework of the interfacial

phenomena involved in different types of functional layers. The work presented in thesis is expected to provide a primary route to the control of the structural organization of diverse organic molecules in solution at the interfaces, the delicate interfacial modification of multi-layers, and the integration of basic building blocks of organic electronics.

Keywords: Organic field-effect transistors, Organic light-emitting transistors, Solution-process, Inkjet printing, Device architecture, Network electrode

Student Number: 2008-20827

Contents

Abstract i

Contents v

List of Figures viii

List of Tables xvi

Chapter 1. Introduction ····· **1**

1.1. Organic Electronics ····· 1

1.2. Organic Field-Effect Transistors ····· 3

1.3. Organic Light-Emitting Transistors ····· 5

1.4. Outline of Thesis ····· 7

Chapter 2. Theoretical Background ····· **9**

2.1. Organic Semiconductors ····· 9

2.2. Interfaces in Organic Electronics ····· 11

2.3. Solution-process for Organic Electronics ····· 14

2.3.1. Physical mechanism of wetting phenomena ····· 15

2.3.2. Inkjet printing technique ····· 17

2.4. Operation of Organic Field-Effect Transistors ····· 20

2.5. Principles of Vertical Organic Light-Emitting Transistors ····· 22

Chapter 3. Leakage Reduction of Solution-processed Organic Field-Effect Transistors ····· 25

3.1. Introduction ····· 25

3.2. Patterned Dielectric Barrier ····· 28

3.2.1. Physical origins of leakage current ····· 28

3.2.2. Fabrication process ····· 29

3.3. Leakage Current Reduction ····· 32

3.4. Electrical characteristics ····· 37

3.5. Summary ····· 39

Chapter 4. Mobility Enhancement of Solution-Processed Organic Field-Effect Transistors ····· 40

4.1. Introduction ····· 40

4.2. Molecular Order by Anisotropic Solvent Drying ····· 43

4.2.1. Thermo-gradient-assisted solvent evaporation ····· 43

4.2.2. Molecular features ····· 46

4.2.3. Electrical characteristics ····· 49

4.3. Topography-Guided Solvent Spreading and Drying ····· 53

4.3.1. Unidirectional topography of inkjet-printed polymer dielectric ····· 53

4.3.2. Analysis of molecular alignment ····· 58

4.3.3. Electrical characteristics ····· 60

4.4. Summary ····· 65

Chapter 5. Quasi-Surface Emissive Organic Light-Emitting Transistors ····· 66

5.1. Introduction ····· 66

5.2. Vertical Structure with Network Source Electrode ····· 68

5.2.1. Structure and fabrication ····· 68

5.2.2. Network source electrode ····· 71

5.3. Quasi-Surface Light Emission ····· 73

5.4. Control of Luminance by Gate Voltage ····· 75

5.5. Summary ····· 79

Chapter 6. Concluding Remarks ····· 80

Appendix (acronyms) 83

Bibliography 85

Publications 95

Abstract (Korean) 105

List of Figures

Figure 1.1. Schematic illustration of typical OFETs in different structures according to the geometrical position of the source and the drain electrodes, organic semiconductor (represented as OSC), gate dielectric, and the gate electrode.·····4

Figure 1.2. Schematic diagram of a lateral-type OLET structure. Two arrows indicate the injection of holes and electrons from the source and the drain electrodes, respectively. Injected charges recombine within the channel in the OSC under control of the gate bias.·····5

Figure 2.1. (a) σ and π bonds in ethylene (C_2H_4), as an simplest example for conjugation system. (b) Energy diagram of ethylene. The sp^2 hybridized and p_z orbitals are combined to form σ and π bonds. The bonding (π) and antibonding (π*) orbitals are indicated. ····· 10

Figure 2.2. (a) Simple electronic structure for the metal-organic (OSC) interface. Φ_m represents the metal work function, E_F the metal Fermi level, E_C the energy level of LUMO corresponding to the conduction band, E_V the energy level of HOMO corresponding to the valence band, and E_g the energy gap between LUMO and HOMO, respectively. (b) Energy band diagram and illustration of hole injection when a positive voltage is applied to the metal electrode. (c) Energy level of the pentacene/Au interface with the positive interface dipole (Δ_{dip}) of 0.6 eV (Ref. [16])····· 12

Figure 2.3. Schematic illustration of a liquid droplet wetting feature on a solid substrate. The contact angle is represented as θ_{CA} and γ_{IJ} denotes the interfacial free energy between phases I and J, including solid (S), liquid (L), and vapor (V) ····· 15

Figure 2.4. (a) Hydrophilic substrate (b) Hydrophobic substrate. DI water droplet on a bare glass and a fluorinated polymer-coated glass, respectively. ····· 16

Figure 2.5. Schematic illustration of drop-on-demand (DOD) inkjet printing system ····· 18

Figure 2.6. (a) Transfer curves and (b) Output curves of a p-type OFET fabricated with pentacene. The electrical parameters such as threshold voltage (V_{th}), on current (I_{on}), on-off current (I_{off}) and subthreshold swing (S) are indicated in (a) ····· 21

Figure 2.7. (a) Cross-sectional and (b) Three-dimensional schematic diagrams of a VOLET structure. Dotted box (red) denotes the aperture in the source electrode. ····· 23

Figure 3.1. Schematic illustration of (a) a typical bottom-gate, top-contact OFET structure with an extra leakage blocking layer on a gate insulator for either the mobility enhancement or the leakage current reduction and (b) a new OFET structure with the PDB for self-pattern registration and low leakage current. The blue arrow and the two red arrows indicate the lateral current (I_L) and two contributions to the vertical current (I_{Vs} across the MISM region and I_{Vd} across the MIM

structure), respectively. The thickness of the PDB is denoted by *t*. (Ref. [64]) ····· 27

Figure 3.2. Simplified equivalent circuit. The variable resistance of MIM region of a gate insulator (GI) and the PDB and the resistance of MISM region are denoted by R_B and R_A, respectively ····· 29

Figure 3.3. (a) The fabrication processes for the OFET with the PDB. (b) The microscopic image of the top-view of the fabricated OFET. The MIM and MISM regions are enclosed by black dashed lines and white dashed lines, respectively. The black arrows represent the pattern boundary of self-registration. (Ref. [64]) ····· 30

Figure 3.4. (a) The current density in the MISM capacitor of Al/PVP/TIPS-pentacene /Au and (b) the current densities in two MIM capacitors of Al/PVP/Au and Al/PVP/fluorinated-polymer/Au as a function of the applied voltage to the Al electrode. Open red triangles and open blue circles represent the current density of Al/PVP/Au and that of Al/PVP/fluorinated-polymer/Au, respectively. (Ref. [64]) ····· 32

Figure 3.5. The capacitance characteristics of the PVP dielectric measured as a function of (a) the frequency and (b) the voltage, respectively. ···· 34

Figure 3.6. The vertical current (open circles) and the lateral current (open triangles) in OFET as a function of the thickness of the PDB. The inset shows the semi-logarithmic plot of ($I_V - I_{V0}$) as a function of *t* below 200 nm. (Ref. [64]) ····· 35

Figure 3.7. The output characteristics measured with varying the gate voltage from 0 V to –5 V in a step of –1 V for (a) the OFET without the PDB and (b) the OFET with the PDB (t = 200 nm). (Ref. [64]) ····· 37

Figure 3.8. The drain current and the gate current at the drain voltage of –5 V as a function of gate voltage. Blue and red symbols represent the drain current and the gate current, respectively. Open circles and open triangles correspond to the OFET with the PDB and the OFET without the PDB, respectively. (Ref. [64]) ····· 38

Figure 4.1. Schematic diagram of a solution-processed TIPS-pentacene-based OFET with a cross-linked PVP insulator. (Ref. [78]) ····· 43

Figure 4.2. Conceptual illustration of (a) conventional solvent evaporation method where the temperature applied to a droplet is constant and (b) temperature gradient-assisted solvent evaporation method ····· 44

Figure 4.3. Schematic diagram showing the underlying concept behind the thermo-gradient-assisted solvent evaporation of a TIPS-pentacene droplet.····· 45

Figure 4.4. The optical microscopic images of the TIPS-pentacene films prepared by (a) the conventional method at 60°C and by the anisotropic solvent drying method at (b) RT-60°C, (c) RT-90°C, and (d) RT-120°C. (Ref. [78])····· 47

Figure 4.5. (a) Typical series of (00l) reflections of the XRD measured for the TIPS-pentacene film generated at RT-90°C condition. (b) The XRD peak intensities as a function of the temperature for the (001) plane in

the TIPS-pentacene films prepared by either temperature-gradient or conventional method. (Ref. [78])····· 48

Figure 4.6. Thickness of TIPS-pentacene film prepared by (a) the conventional drying and (b) the anisotropic solvent drying. ····· 49

Figure 4.7. The output characteristic curves of four OFETs. The TIPS-pentacene film was prepared by (a) a conventional solvent drying method at 60°C and by the anisotropic solvent drying method at (b) RT-60°C, (c) RT-90°C, and (d) RT-120°C. The curves were obtained with varying the gate voltage from 0 V to -50 V in a step of -10 V. (Ref. [78])····· 50

Figure 4.8. The transfer characteristic curves of four types of OFETs. Open circles, triangles, squares, and diamonds represent the conventional solvent drying case, anisotropic solvent drying case at RT-60°C, RT-90°C, and RT-120°C, respectively. The data at the drain voltage of -50V was used for obtaining the mobility of OFETs. (b) Magnitude of both the mobility and the off current in each OFET as a function of the temperature-gradient between a heat reservoir fixed at RT and a temperature variable hot-plate. Open circles and squares represent the mobility and the off current, respectively. (Ref. [78]) ····· 51

Figure 4.9. Schematic diagram showing the construction of UT of PVP on top of the uniform PVP insulator by inkjet printing. The radius of a single PVP droplet and the printing pitch are denoted by *r* and *p*, respectively. The width and the height of the ridge formed by a series of the droplets printed in line are *w* and *h*, respectively. The center-to-center

distance between two adjacent ridges is *d*. The inset is the optical microscopic image of a single PVP droplet pattern showing the coffee-ring effect. (Ref. [86]) ····· 54

Figure 4.10. The optical microscopic image of PVP ridges constructed on the uniform PVP layer by inkjet printing and the geometrical profiles of several PVP ridges. The *x*-axis and *y*-axis are defined as the directions perpendicular and parallel to UT, respectively. (Ref. [86])····· 55

Figure 4.11. The contact angles of water on (a) the uniform PVP insulator prepared by spin-coating (θ_s), (b) on PVP insulator with the UT measured along the *y*-axis ($\theta_\perp$), and (c) on PVP insulator with UT measured along the *x*-axis ($\theta_\parallel$). (d) The schematic illustration of an elongated TIPS-pentacene droplet formed on PVP insulator with UT by anisotropic wetting. The black dashed arrows indicate the directions of preferential spreading of the droplet along the ridges. The optical microscopic images of the TIPS-pentacene films prepared (e) on a uniform PVP film and (f) on PVP with UT. The radial domains on the uniform PVP and the elongated, bilateral domains along UT of PVP are indicated by black solid arrows. (Ref. [86]) ····· 57

Figure 4.12. (a) The experimental setup for the measurements of the optical anisotropy. The optical retardation values for (b) the uniform PVP (open circles) and PVP with UT (filled circles), (c) TIPS-pentacene film on the uniform PVP, and (d) TIPS-pentacene film on PVP with UT. (Ref. [86])····· 59

Figure 4.13. Schematic diagram showing a TIPS-pentacene OFET on PVP insulator with UT in a bottom-gate, top-contact configuration. (Ref. [86]) ····· 61

Figure 4.14. (a) The output characteristics as a function of drain voltage for the gate voltages of –10 V (solid lines), –30 V (dotted lines), and –50 V (dashed lines) for three OFETs on the uniform PVP (black lines), on PVP with UT perpendicular to the channel (red lines), and on PVP with UT parallel to the channel (blue lines). (b) The transfer curves for the three cases as a function of the gate voltage at the drain voltage of –50 V. The insets are the optical microscopic images of the channel regions for the three cases. Histograms showing the distribution of (c) the current on-off ratio values and (d) that of the mobility values for the three cases. (Ref. [86]) ····· 62

Figure 5.1. Cross-sectional view of our VOLET with a network source electrode having periodic apertures. The lateral charge transport (q_L) and the vertical charge transport (q_V) are depicted as solid and dashed arrows, respectively. ····· 68

Figure 5.2. Illustration of our VOLET architecture with a network source electrode and the stacked layers of functional materials. ····· 69

Figure 5.3. Fabrication procedure of the network source electrode by conventional photolithography and the dry (or wet) etching ····· 70

Figure 5.4. Microscopic images of three network source electrodes, having different sizes of the apertures, covered with the PVP layers. The size of each aperture and the separation between two adjacent apertures

were denoted by W_a and W_e, respectively. The value of W_a = W_e was varied to be (a) 20 μm, (b) 10 μm, and (c) 5 μm. ····· 71

Figure 5.5. Microscopic images for the light emission through the apertures of the network source electrode in three VOLETs with different values of (a) W_a = 20 μm, (b) W_a = 10 μm, and (c) W_a = 5 μm at the drain voltage of –10 V and the gate voltage of –10 V under zero source voltage. (d) Intensity profiles along the yellow line across a single aperture for each OLET given in (a)-(c). Green, blue, and red colors represent W_a = 20, 10, and 5 μm, respectively. In each case, the FWHM (depicted by the gray arrow) was estimated from two intensity curves separated from one another by extrapolation. ····· 74

Figure 5.6. Light emission features through 6 × 6 apertures of W_a = 5 μm in the source electrode at the gate voltage of (a) –50 V, (b) 0 V, and (c) +50 V at the drain voltage of –10 V. ····· 76

Figure 5.7. (a) Electroluminescence (EL) spectra of the emitted light (b) Color location (x = 0.313 and y = 0.555) on the CIE 1931 color space chromaticity diagram. ····· 76

Figure 5.8. Luminance as a function of the gate voltage. The inset shows a photograph together with a zoom-in microscopic image for the light emission from the OLET (2.5 mm × 2 mm in size) with 50,000 apertures in the source electrode at the gate voltage of –50 V and the drain voltage of –10 V. ····· 77

List of Tables

Table 3.1. The physical properties of EGC-1700 ····· 31

Table 4.1. The electrical performances (mobility, on/off current ratio, V_{th}) for three structures····· 64

Chapter 1. Introduction

1.1. Organic Electronics

The progress in the performance and physical understanding of both organic materials and devices has been prompted by the enormous interests to realize a new class of electronic applications. In addition to the intrinsic advantages of organic semiconductors such as the versatile processing capability and the flexibility in design, the recent advances in the electrical performance have led to the advent of a great deal of organic electronics including flexible and large-area electronics, low-cost printed electronics, and optoelectronics. As one of the representative organic electronics, organic light-emitting diodes (OLEDs) are widely used for displays technology in commercialized products such as smartphones and high-definition televisions. Organic photovoltaic (OPV) cells also continue to improve and theoretical efficiency achievable in practical devices is estimated to meet the level required in consumer markets. Among them, organic field-effect transistors (OFETs) are expected to serve as key elements for the practical applications such as flexible displays, smart cards, radio-frequency identification tags, and sensors.

In development of such organic electronic devices, it is primarily important to understand the underlying physics associated with charge transport mechanism and the structural organization of organic molecules directly which influence on the electrical properties of organic

semiconductors. Secondly, it should be highlighted that organic electronic devices basically consist of multi-layers with the different patterns, which inevitably generate a variety of interfaces involving complex physicochemical phenomena. Thus, the control of interfacial interactions between organic and/or inorganic materials as well as the layer-by-layer engineering are significant to provide a primary route to the observation of physical phenomena and the development of novel electronic systems.

In this chapter, the two types of organic electronic devices discussed throughout this thesis, one of which is OFET providing both switching and driving capabilities and the other is organic light-emitting transistor (OLET) possessing the light-generating capability together with the electrical switching functionality, are introduced briefly.

1.2. Organic Field-Effect Transistors

OFETs are considered as a key component of organic integrated circuits due to their switching and driving capabilities as mentioned in **Section 1.1**. In the past decade, much effort has been made in developing a variety of organic semiconducting materials [1], devising new OFET device structures [2], and modifying interfacial interactions [3]. Recently, the electrical properties of OFETs have even exceeded those of an amorphous silicon-based FET at a performance level for microelectronic applications.

A typical OFET is composed of a gate electrode which is separated from an organic semiconductor by a gate dielectric layer and the source/drain electrodes. Both the architecture and operating principles of OFETs are based on the device model of metal-oxide-semiconductor FET, even though they can be specifically classified in different structures according to the geometrical position of each component as illustrated in Fig. 1.1.

For the transistor operation, in case of p-type OFETs, the holes are injected from the source electrode into the organic semiconductor and accumulated in the vicinity of the organic-dielectric interface under the negative gate bias and then the charges migrate through the channel, generating the current flow, by an electric field between the source and the drain electrodes. The gate voltage is modulated to switch the OFET on and off.

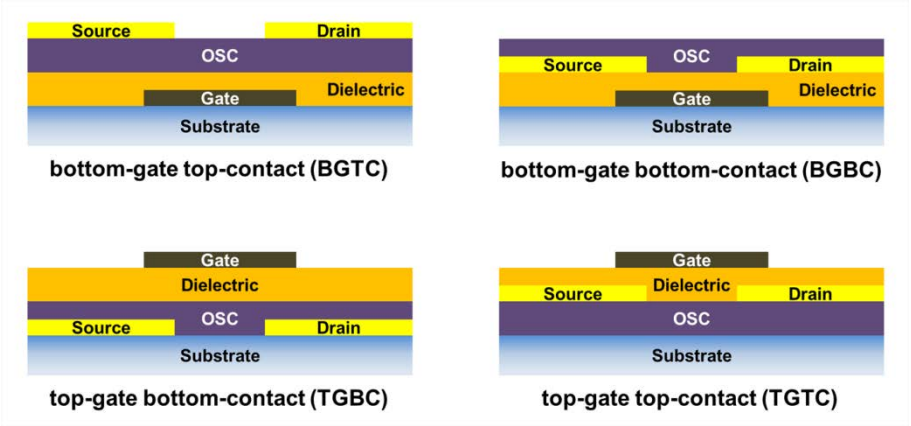

Figure 1.1. Schematic illustration of typical OFETs in different structures according to the geometrical position of the source and the drain electrodes, organic semiconductor (represented as OSC), gate dielectric, and the gate electrode.

For high performance of OFETs, the inherent properties of organic semiconducting materials themselves are mostly important, but device architectures, interfacial properties at organic-dielectric and/or organic-metal, and fabrication methods should be also taken into account. Particularly, engineering of each functional layer in such multi-layers structure is of great relevance for the development of advanced electronic and/or optoelectronic systems.

1.3. Organic Light-Emitting Transistors

OLETs that simultaneously possess the light-emitting capability and the electrical switching property of transistors have attracted tremendous interest for fundamental studies in organic electronics and advanced technological applications [4, 5]. OLETs have an enormous potential being as multifunctional optoelectronic devices beyond OLEDs due to a high aperture ratio and high quantum efficiency compared to OLEDs [6]. Most of OLETs has been typically developed in a planar geometry in which a source electrode and a drain electrode are laterally constructed as shown in Fig. 1.2 [7-9]. In this structure, they can provide the visualized scheme for understanding the physical mechanism such as charge carrier injection, transport, and recombination in a semiconductor layer [10]. An OLET has a three-terminal architecture so that charge injection and recombination are controlled in an electrical scheme in contrast to OLEDs where charge behaviors are mainly affected by the properties of the multi-layered materials.

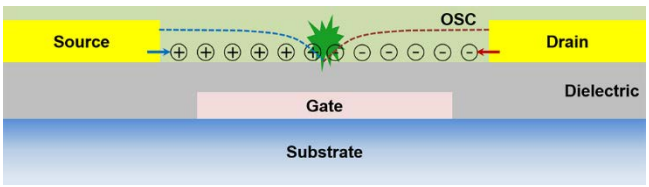

Figure 1.2. Schematic diagram of a lateral-type OLET structure. Two arrows indicate the injection of holes and electrons from the source and the drain electrodes, respectively. Injected charges recombine within the channel in the OSC under control of the gate bias.

In lateral-type OLETs, both charge carriers of holes and electrons are injected from the source and the drain contacts by controlling the energy barrier at the organic-metal interface with the help of the gate bias. Then, the recombination of holes and electrons moving within the channel region and consequent electroluminescence intensity are tuned by both the drain and the gate voltage. Note that essential prerequisites, (i) efficient injection for both holes and electrons at the electrodes; (ii) ambipolar field-effect transporting and light-emitting ability of the active layer, should be guaranteed for the distinct device characteristics of OLETs.

Even though OLETs clearly have the advantages beyond OLEDs in terms of the electroluminescence quantum efficiency and the aperture ratio [4], one has to bear in mind that the light emission area in the lateral-type OLETs is not sufficient to be utilized in practical applications owing to the intrinsic line emission characteristics. Although several approaches using an interdigitated electrode or a trilayer active heterostructure have been attempted to expand the effective light emission area out of the entire device [11, 12], the emission area obtained by such additive manner of line emission is still limited since the line emission is confined in only a few hundreds of nanometers [4]. Therefore, the novel class of architecture is strongly required, and this is discussed in **Section 2.5** and **Chapter 5** in detail.

1.4. Outline of Thesis

This thesis contains six chapters including this **Introduction** and **Concluding Remarks**. In **Chapter 1**, both OFETs and OLETs are briefly introduced, and the distinct issues concerning the engineering of functional layer and the device architecture for developing the advanced organic electronic devices are addressed. **Chapter 2** explains the theoretical background with regard to the charge transport in organic semiconductors and the underlying mechanism at the interfaces in organic electronics. The fabrication method focusing on the solution-process such as an inkjet printing with the related fundamental physics are introduced. The general operating principles of OFET and vertical OLET (VOLET) are also described. The scientific and engineering approaches for developing advanced OFETs and OLETs are demonstrated by dividing into two major categories, one of which is focusing on the solution-processed OFETs in **Chapter 3** and **Chapter 4** and the other is vertical OLETs (VOLETs) showing the quasi-surface emission in **Chapter 5**. In **Chapter 3**, a new type of a solution-processed OFET, which leads to low leakage current and self-pattern registration, based on a patterned dielectric barrier (PDB) is demonstrated. The PDB of a hydrophobic fluoro-polymer enables to effectively reduce the vertical charge flow generated from the gate electrode as well as defines spontaneously an active channel pattern by means of the selective wettability and the geometrical confinement. **Chapter 4** contains two viable methods of inducing the molecular order of solution-processed organic semiconductor for mobility enhancement by

controlling the solvent spreading and drying. First, a control scheme of the molecular order and cracks in a solution-processed organic semiconductor film on a polymeric insulator by the temperature gradient during the solvent drying process is introduced. Secondly, the enhancement of the field-effect mobility of solution-processed OFET by unidirectional topography (UT) of an inkjet-printed polymer insulator is reported. The UT leads to anisotropic spreading and drying of the TIPS-pentacene droplet and enables to spontaneously develop the ordered structures during the solvent evaporation. In **Chapter 5**, VOLET with a network electrode of closed topology for quasi-surface emission is demonstrated. The spatial distribution of the surface emission depends primarily on the relative scale of the aperture in the network electrode to the characteristic length for the charge carrier recombination. Due to the closed topology in the network of the source electrode, the charge transport and the resultant carrier recombination are substantially extended from individual network boundaries toward the corresponding aperture centers in the source electrode. The luminance was found to be well-controlled by the gate voltage through an organic semiconducting layer over the network source electrode. Finally, **Chapter 6** provides a summary and concluding remarks.

Chapter 2. Theoretical Background

2.1. Organic Semiconductors

Organic semiconductors are based on sp^2 hybridized carbons resulting in three σ bonds and a conjugated π bond being formed by the remaining p_z orbital. Figure 2.1(a) shows the σ and π bonds in ethylene (C_2H_4) as a simplest example. Under this scheme, since the π bonding is significantly weaker than the σ bonds, the energy gap between the bonding (π) and antibonding (π*) orbitals is reduced in comparison to the materials involving only σ bonds as shown in Fig. 2.1(b) [13, 14]. In case of a chain of carbon atoms, where the each carbon is linked to neighboring carbon atoms, it consists of alternating single and double bonds, namely the conjugation system. When the conjugation length is increased for the larger molecules, the delocalization of π orbitals is enhanced, resulting in the smaller energy gap defined as the distance between highest occupied molecular orbitals (HOMO) and lowest unoccupied molecular orbitals (LUMO). Thus, the delocalized electrons in the π bonds can give rise to charge carrier mobility showing the semiconductor behavior. It is generally known that charge transport in organic semiconductors occurs via a hopping mechanism which is activated by thermal energy, in contrast to the crystalline inorganic material based on the band transport theory [15].

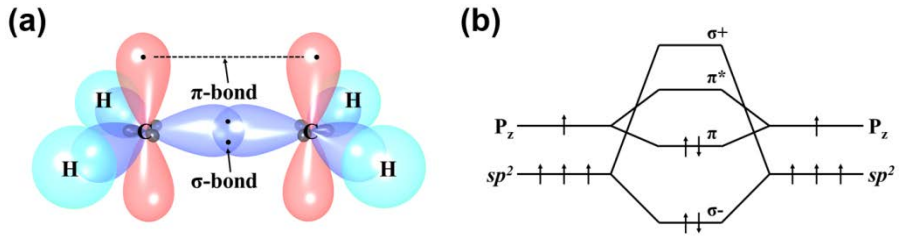

Figure 2.1. (a) σ and π bonds in ethylene (C_2H_4), as an simplest example for conjugation system. (b) Energy diagram of ethylene. The sp^2 hybridized and p_z orbitals are combined to form σ and π bonds. The bonding (π) and antibonding (π*) orbitals are indicated.

In other words, the charge transport in organic molecules is governed by the delocalization of electronic wavefunctions between neighboring molecules as well as the intramolecular delocalization. Particularly, in OFETs where charges propagate along the channel of micrometer scale, charge transport (or mobility) is considered the most crucial factor to achieve the desired electrical characteristics. Thus, it is significant to align the molecules of organic semiconductor into closely packed organization so that the intermolecular π orbitals overlap can be maximized for the efficient charge transport.

2.2. Interfaces in Organic Electronics

Besides the organic semiconductor itself, the interfacial properties of organic electronic devices also play a critical role for the electrical performance and the operating stability. The interfaces generated in organic electronic devices can be broadly divided into two aspects, one of which is the interface at organic-metal and the other is at organic-organic. In typical organic electronics such as OLEDs, OPVs, and OFETs, metal electrodes contacting the organic semiconductor are used for charge injection into or charge extraction from the organic semiconductor. Thus, it is required the energy level alignment between the metal work function (Φ_m) and HOMO level (E_V) (or LUMO level (E_C)) of the organic semiconductor to reduce the contact resistance which directly influence on charge injection and extraction [15].

Figure 2.2(a) shows the simple electronic structure for the metal-organic interface where the difference of $E_F - E_V$ essentially refers to the potential barrier for hole injection in case of p-type organic semiconductor. Note that this barrier can be controlled by applying a bias to the metal and the holes can be injected into the organic semiconductor when a positive bias is applied to the metal relative to the organic semiconductor as depicted in the energy band diagram in Fig. 2.2(b). However, the electronic structure at the interface in reality is somewhat different due to the complex interaction phenomena such as induced dipoles and resultant polarization effects as illustrated in Fig. 2.2(c) for an example of gold (Au) and pentacene interface [16]. Therefore, the relevant engineering of the metal-organic interface as well as the energy level

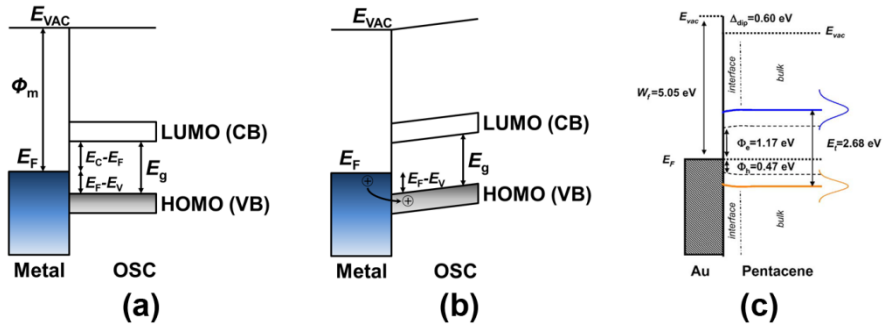

Figure 2.2. (a) Simple electronic structure for the metal-organic (OSC) interface. Φ_m represents the metal work function, E_F the metal Fermi level, E_C the energy level of LUMO corresponding to the conduction band, E_V the energy level of HOMO corresponding to the valence band, and E_g the energy gap between LUMO and HOMO, respectively. (b) Energy band diagram and illustration of hole injection when a positive voltage is applied to the metal electrode. (c) Energy level of the pentacene/Au interface with the positive interface dipole (Δ_{dip}) of 0.6 eV (Ref. [16])

alignment is significant to optimize charge carrier behavior including injection, transport, and recombination and to improve the electrical performance of organic electronics.

In the organic electronic devices composed of multi-layers, the organic-organic interface is no less important than the organic-metal interface. In OLEDs and OPVs, both charge carriers, the electron and the hole, flow through the organic-organic interface, and this transport process mainly governs the device operation involving charge recombination and dissociation. In case of OFETs, of particular importance is to understand the underlying physics and the phenomena at the interface between organic semiconductor and polymeric gate dielectrics since they critically influence on the electrical

parameters of the OFETs such as mobility, threshold voltage, and hysteresis. For engineering of the organic-dielectric interface, numerous approaches such as deposition of self-assembled monolayer [17], exposure to ultraviolet ozone [18] and/or plasma [19], and introduction of the buffer layer [20] have been introduced. As mentioned in the previous section, the efficient charge transport can be promoted by closely packed organization of the organic semiconductor. Considering that the molecular alignment is dominantly affected by the surface properties of dielectric, the adequate interfacial tailoring and/or engineering can induce the enhancement of charge transport.

2.3. Solution-process for Organic Electronics

The intermolecular interaction of organic semiconductors is relatively weak compared to inorganic materials having a covalent bonding structure. This property results in the mechanical and thermodynamic vulnerability, but it also provides a broad range of strategies for manipulating organic semiconductors and fabricating organic electronics. Thermal evaporation (or vacuum deposition), one of the most widely used deposition techniques, is to evaporate the molecules, and then to condense the vapor phase into the solid phase on the target substrate. However, it is applicable to only small molecules for instance pentacene, and places a limit on large-area applications due to geometrical boundaries such as the size of vacuum chamber. As an alternative, solution-process has been extensively investigated for flexible, large-area, and low-cost electronic applications [21-23] owing to the capability of low temperature processing and the simplicity in fabrication by versatile printing methods, for example, roll-to-roll processing, and inkjet printing [24-27]. During the solution-process, since it basically involves spreading and drying of a liquid on a solid surface, the interaction at the solid/liquid interfaces as well as the thermodynamic behavior of a liquid should be understood. Particularly, in case of organic semiconductors including polymers and oligomers, physicochemical properties of solvent and solution-processing conditions in addition to intrinsic molecular properties considerably also influence on mesoscale morphology, crystallinity, and molecular orientation in a deposited film that play a critical role for the charge

transport in organic electronic devices [15]. This section aims to discuss the physical mechanism of wetting phenomena of a liquid droplet on a solid surface, and to review the printing techniques focusing on inkjet printing.

2.3.1. Physical mechanism of wetting phenomena

Wetting essentially refers to the spreading phenomena of a liquid deposited on a solid substrate. When a liquid droplet is in contact with a smooth and homogeneous solid substrate, the droplet forms a spherical cap with a characteristic angle, namely contact angle, at thermodynamic equilibrium minimizing the total free energy as illustrated in Fig. 2.3 [28]. This contact angle (θ_{CA}) is commonly used to investigate the wetting (or dewetting) property in a quantitative manner, and normally given by Young's equation:

$$\gamma_{LV} \cos\theta_{CA} = \gamma_{SV} - \gamma_{SL} \tag{2.1}$$

where γ_{IJ} denotes the interfacial free energy between different phases I and J, including solid (S), liquid (L), and vapor (V).

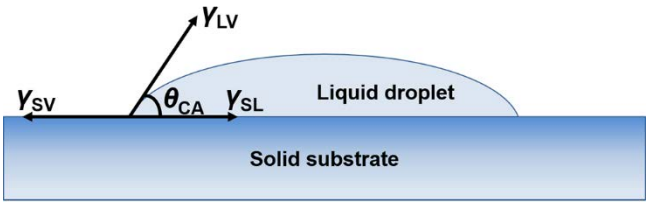

Figure 2.3. Schematic illustration of a liquid droplet wetting feature on a solid substrate. The contact angle is represented as θ_{CA} and γ_{IJ} denotes the interfacial free energy between phases I and J, including solid (S), liquid (L), and vapor (V)

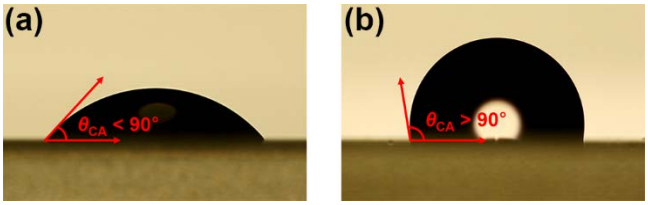

Figure 2.4. (a) Hydrophilic substrate (b) Hydrophobic substrate. DI water droplet on a bare glass and a fluorinated polymer-coated glass, respectively.

In general, the substrate is simply classified into two wetting criteria, hydrophilic ($\theta_{CA} < 90°$) and hydrophobic ($\theta_{CA} > 90°$), according to the contact angle of a deionized (DI) water droplet on it. Figure 2.4(a) and 2.4(b) show the DI water droplet features on a bare glass and a fluorinated polymer-coated glass as examples for hydrophilic and hydrophobic substrates, respectively.

However, on the textured surface, the wetting behaviors deviate from the equilibrium on the smooth surface, and can be usually explained by either Wenzel's model [29] or Cassie-Baxter's model [30]. Especially, when the textured structure is chemically homogeneous and the roughness scale is small enough to neglect the air fraction at the interface between water and surface, the equilibrium condition leads to Wenzel's relation, which is expressed as

$$\cos\theta_a = k\cos\theta_{CA} \tag{2.2}$$

where θ_a is apparent angle and k is a constant depending on the ratio of the effective surface area in contact with the liquid to the projected surface area. This Wenzel's model manifests following wetting behaviors: (i) if $\theta_{CA} < 90°$ (hydrophilic), $\theta_a < \theta_{CA}$; and (ii) if $\theta_{CA} > 90°$ (hydrophobic), $\theta_a > \theta_{CA}$; for k which is fundamentally larger than unity. In other words, surface textures

always reinforce the both hydrophilic and hydrophobic wetting properties [31]. Regarding that the molecular alignment in solution-process is affected by spreading and drying behaviors of solvent and the surface properties of dielectric, physical mechanism of wetting phenomena introduced in this section should be emphasized for the enhancement of charge transport and electrical performance of organic electronic devices.

2.3.2. Inkjet printing technique

For the fabrication of conventional electronic systems, the subtractive methods including photolithography and dry (or wet) etching have been widely used. Even though those techniques have been continually developed so that the pattern features are reduced to a level of tens of nanometers with high density, they suffer from high manufacturing costs and limited throughput due to the numerous complicated steps. In contrast, printing techniques based on an additive fashion theoretically require only a single step for fabricating a single layer. Among them, inkjet printing has been increasingly important for the emerging printable electronics on a variety of substrates, being flexible and/or stretchable, to dramatically reduce the material waste and the production cost [32-34]. Since inkjet printing allows a wide range of fluidic characteristics in terms of viscosity and chemical nature for inkjet materials, it is of great advantage to produce a number of solution-process organic semiconductors compatible with inkjet printing.

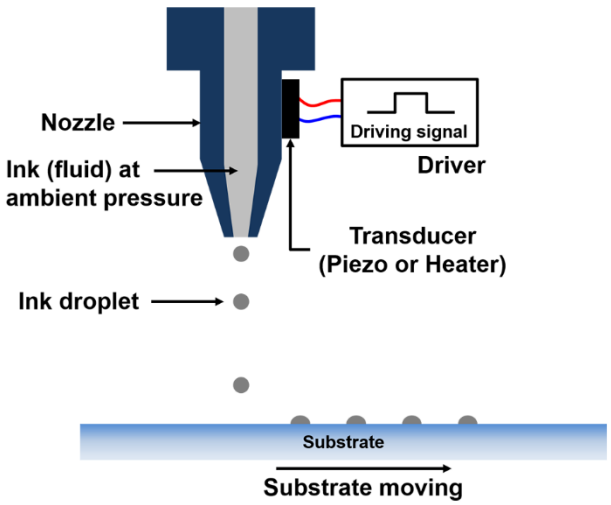

Figure 2.5. Schematic illustration of drop-on-demand (DOD) inkjet printing system

Figure 2.5 shows drop-on-demand (DOD) inkjet printing system, one of the most promising inkjet technologies, in which literally ink droplets are ejected when demanded. In this system, either heating a resistive element causing formation of vapor bubbles or applying a voltage wave to a piezoelectric transducer is typically utilized to create a pressure pulse and to ultimately eject the droplets through the nozzle orifice [35]. In case of piezoelectric DOD inkjet printing, it provides high degree of freedom for ink development, and avoids from ink degradation concerns unlike the thermal inkjet system [14].

One of the important requirements for realizing organic electronic devices by inkjet printing is to build up multi-layers with accurate pattern registration and solvent orthogonality, because most of organic electronics are composed of multi-layers as mentioned in **Sections 1.2** and **2.2**. By inkjet

printing, generally, it is inherently difficult to control the printed features such as morphology, edge shape, line width, and thickness due to the nature of liquid, resulting in for example a relatively large overlap capacitance in printed organic electronic devices. As one of the approaches to achieve the high resolution and pattern fidelity, self-alignment between multi-layers by exploiting wetting properties has been demonstrated [32, 36]. Overall, thus, understanding of fluid behaviors together with the improvement of inkjet printing technique itself should be appropriately accompanied to develop and optimize printed electronics.

2.4. Operation of Organic Field-Effect Transistors

Figure 2.6(a) and 2.6(b) show the transfer curves and the output curves, for a p-channel OFET, representing the electrical characteristics in terms of drain current behavior as a function of the gate voltage and the drain voltage, respectively. The operation parameters such as field-effect mobility (μ), threshold voltage (V_{th}), on/off current ratio (I_{on}/I_{off}) and subthreshold swing (S) can be extracted from the transfer curves as shown in Fig. 2.6(a). Here, I_{on} and I_{off} is defined as the values of the maximum and the minimum drain current, respectively, and V_{th} is the intercept of the extrapolation of the square root of the drain current on the gate voltage axis. Subthrehold swing is the inverse value of slope of the logarithmic drain current. The output curves plotted in Fig. 2.6(b) shows the OFET operating in the linear regime and the saturation regime with respect to V_D. The drain current in the linear regime where $|V_D| < |V_G - V_{th}|$ and $|V_G| > |V_{th}|$ is given by [37]

$$I_D = \frac{W}{2L}\mu C_i[(V_G - V_{th})V_D - \frac{1}{2}{V_G}^2] \quad (2.3)$$

where L and W are the length and the width of channel, respectively. Here, C_i represents the capacitance of a gate insulator per unit area, I_D the drain current, V_D the drain voltage, and V_G the gate voltage. The drain current in the saturation regime where $|V_D| > |V_G - V_{th}|$ is

$$I_D = \frac{W}{2L} C_i \mu (V_G - V_{th})^2 \quad (2.4)$$

The operation principles for an n-channel OFET are fundamentally similar to the p-channel, adopting the electrons controlled by a positive bias as charge

carriers and taking analogous biasing conditions into account. Note that the high-performance, ambient-stable n-type organic semiconductors have gradually attracted interests for realizing complementary circuits which can derive high circuit speeds, low power dissipation, and stable operation [21].

From the transfer characteristic curves as shown in Fig. 2.6(a) and Eq. (2.4), the field-effect mobility in the saturation region is theoretically extracted by the following equation [38]:

$$\mu = \frac{2L}{WC_{\mathrm{i}}}\left(\frac{\partial\sqrt{I_{\mathrm{D}}}}{\partial V_{\mathrm{G}}}\right)^2 \tag{2.5}$$

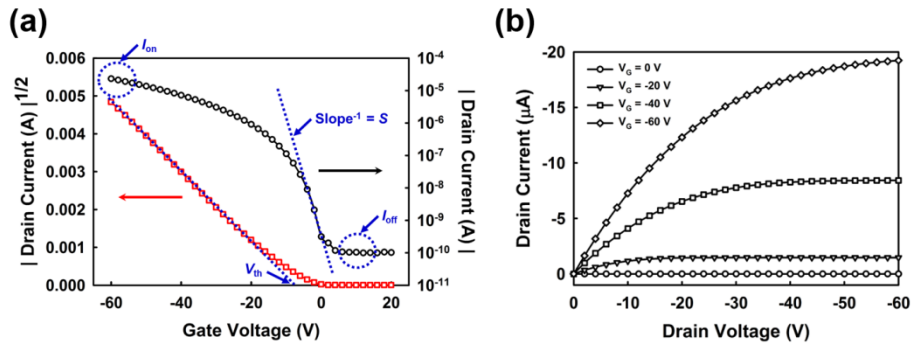

Figure 2.6. (a) Transfer curves and (b) Output curves of a p-type OFET fabricated with pentacene. The electrical parameters such as threshold voltage (V_{th}), on current (I_{on}), on-off current (I_{off}) and subthreshold swing (S) are indicated in (a)

2.5. Principles of Vertical Organic Light-Emitting Transistors

As pointed out in **Section 1.3**, even though OLETs have indisputable intrinsic merits, line-type emission characteristics are inevitable in lateral-type OLETs where a source electrode and a drain electrode are laterally located on the same plane. In other words, effective light emission occupies only a small region out of the entire device. In order to overcome this limitation, recently, vertically stacked architectures have been suggested [39-41]. For understanding of fundamental mechanisms of VOLETs, operating principles of vertical organic field-effect transistors (VOFETs) can be exploited. VOFETs have been generally studied to improve electrical performances such as the mobility, operating frequency, and power consumption [42-45], but they can also serve as building blocks for the development of VOLETs having a large emission area and high resolution in integrated circuits [46].

In VOLETs, charge injection mechanism at organic-metal interface is basically identical with the typical OFETs case which is discussed in **Section 2.2**. The HOMO level of organic semiconductor should be lie within a range of the metal work function (or the Fermi level) that can be controlled by rationally applicable gate voltage. For a p-type organic semiconductor, the positive gate voltage suppresses the charge injection by generating the effective potential barrier, and the negative gate voltage lowers the potential barrier with an induced electric field. One remarkable difference in VOLET is

that it is greatly important to prevent screening an electric field from the gate electrode so as to control the energy barrier at organic-metal interface and thus the source electrode should contain the apertures. After the charges are injected from the metal contacts, an electric field between the drain and the source electrodes induces the holes- and electrons-flow in the opposite direction, resulting in the charge recombination in the emission layer as depicted in Fig. 2.7(a). Here, charge injection from the source contact and the current between the source and the drain electrodes can be described by the filed-enhanced thermionic emission theory and the space charge limited current theory, respectively [44]. Here, assuming that the energy barrier at the source electrode and organic semiconductor is not high enough to block direct charge injection and transport occurring irrespective of the gate voltage between the source and the drain electrodes, the insulator should be formed on the source electrode. Otherwise, devices are not properly switched off, degrading the on/off current ratio.

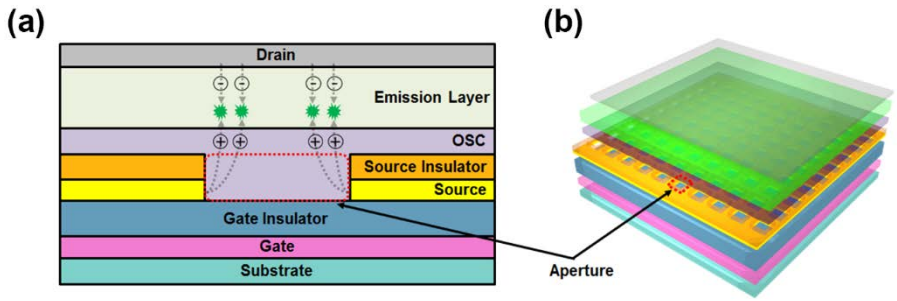

Figure 2.7. (a) Cross-sectional and (b) Three-dimensional schematic diagrams of a VOLET structure. Dotted box (red) denotes the aperture in the source electrode.

From the viewpoint of the emission area, the actual emission should be maximized in the apertures in order to obtain the comparable level of commercialized OLED. Here, it is worth to note that the spatial distribution of light emission is primarily governed by charge transport in the horizontal direction from each side of apertures even though charge recombination in the emission layer is mainly limited by charge transport in the vertical direction. Therefore, the systematic analysis of light-emitting characteristics depending on the size and/or the ratio of apertures in electrode should be carried out to comprehensively understand the charge carrier behaviors and to expand the emission area.

Chapter 3. Leakage Reduction of Solution-processed Organic Field-Effect Transistors

3.1. Introduction

Although the electrical properties of solution-processed OFETs have been remarkably progressed, approaching those of amorphous silicon-based FETs, large leakage current which causes the low on-off current ratio and deteriorates the operating stability is still considered as one of the detrimental problems [47]. It is generally known that the magnitude of the leakage current is strongly influenced by a gate dielectric material itself as well as the interfacial changes between the dielectric layer and an active layer including the surface morphology [48, 49], impurities [50], and the physicochemical interactions [51, 52]. For conventional OFETs fabricated by vacuum deposition, a new type of a dielectric material, for example, an ultrathin cross-linked blend [53], can be simply used as a gate insulator, or extra leakage blocking layer such as an organic-inorganic hybrid layer [54] and a self-assembled monolayer (SAM) [55] can be employed onto a gate insulator for reducing the leakage current as shown in Fig. 3.1(a). However, for solution-processed OFETs, it has been a serious challenge to reduce the leakage current since different solvents for successive solution processes may alter the intrinsic physical and/or chemical properties of underlying layers in the OFETs. In other words, a proper selection of mutually inert materials and

solvents is an important issue on the preservation of different functional layers during the subsequent solution process.

Another issue is how to precisely pattern a soluble organic semiconductor (OSC) in channel regions for eliminating the crosstalk between neighboring OFET elements in an integrated circuits array. For soluble OSCs, direct patterning such as inkjet printing [56] or transfer printing [57] is commonly utilized due to the processing simplicity while indirect pattering by physical delamination [58], self-organization on the SAMs [59-61], or bank structures [62, 63] is often used for achieving high resolution and high level of integration. In fact, patterned organic semiconductor layers on a gate insulator enable to prevent undesired current pathways and thus are capable of reducing the off-current without sacrificing the mobility. Therefore, it is extremely important to develop a new OFET architecture suitable for solution-processing of the organic semiconductor and the gate insulator from the viewpoints of both the feature resolution and the chemical compatibility.

In this chapter, a new concept of using a PDB is introduced to simultaneously achieve the reduction of the leakage current and the self-pattern registration of solution-processed OFETs in a bottom-gate, top-contact geometry as shown in Fig. 3.1(b). The PDB of a hydrophobic fluorinated-polymer was prepared on a gate insulator by transfer printing with a pre-patterned elastomeric stamp. The PDB leaves a cavity resembling a via-hole structure for an active region to facilitate self-pattern registration of a solution-processed organic semiconductor. In this PDB configuration, as the PDB thickness increases, the vertical charge flow between the gate and the

drain becomes essentially screened out, meaning that the vertical current is tremendously reduced. Moreover, the selective wetting properties of the PDB allow to spontaneously pattern a solution of the OSC into the cavity like a via-hole structure.

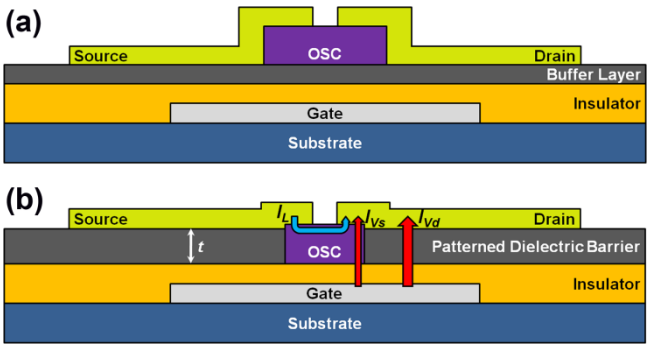

Figure 3.1. Schematic illustration of (a) a typical bottom-gate, top-contact OFET structure with an extra leakage blocking layer on a gate insulator for either the mobility enhancement or the leakage current reduction and (b) a new OFET structure with the PDB for self-pattern registration and low leakage current. The blue arrow and the two red arrows indicate the lateral current (I_L) and two contributions to the vertical current (I_{Vs} across the MISM region and I_{Vd} across the MIM structure), respectively. The thickness of the PDB is denoted by *t*. (Ref. [64])

3.2. Patterned Dielectric Barrier

3.2.1. Physical origins of leakage current

In general, the leakage current in an OFET comes from two physical origins, one of which is the lateral current (I_L) through the organic semiconductor from the source electrode to the drain electrode and the other is the vertical current through the gate insulator from the gate electrode to the drain electrode. More specifically, the vertical current consists of the current through a metal-insulator-semiconductor-metal (MISM) structure (I_{Vs}) and a metal-insulator-metal (MIM) structure (I_{Vd}). Note that the latter is a major contribution to the leakage current, and it depends strongly on the dielectric properties of the PDB. In contrast to Fig. 3.1(a) where a gate insulator is entirely covered with a buffer layer, the organic semiconductor in Fig. 3.1(b) is directly in contact with a gate insulator. Thus, the lateral current is essentially independent of the presence of the PDB.

As the thickness of the PDB increases, it can be expected that the resistance of MIM region consisted of a gate insulator and the PDB (R_B) would also increase, while the resistance of MISM region (R_A) is constant. Thus, the leakage current mainly flows through R_B at first, but it is gradually governed by R_A after the point of $R_A < R_B$. The simplified equivalent circuit describing R_A and R_B is shown in Fig. 3.2.

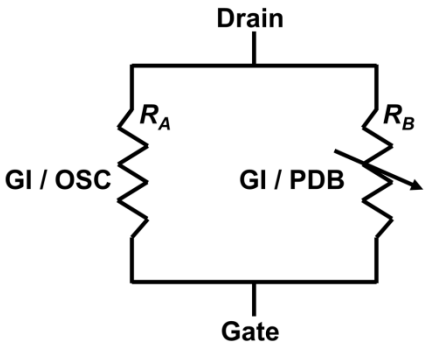

Figure 3.2. Simplified equivalent circuit. The variable resistance of MIM region of a gate insulator (GI) and the PDB and the resistance of MISM region are denoted by R_B and R_A, respectively

3.2.2. Fabrication process

The fabrication processes for the OFET with the PDB and the microscopic image of the fabricated OFET are shown in Figs. 3.3(a) and 3.3(b), respectively. The elastomeric stamp having desired patterns of the dielectric barrier, complementary to the organic semiconductor patterns, was made of poly(dimethylsioxane) (PDMS) (Sylgard 184, Dow Corning). As shown in Fig. 3.3(a), the receiving substrate had a gate electrode (aluminum: Al) of 60 nm thick on which a gate insulator, poly(4-vinylphenol) (PVP) mixed with methylated poly(melamine-co-formaldehyde) (MMF) (100 wt.% of PVP) in propylene glycol methyl ether acetate (PGMEA) in 5 wt.%, was coated by spin-coating at 3000 rpm for 30 sec. The gate insulator was 100 nm thick after the subsequent thermal cross-linking at 200°C for 30 min.

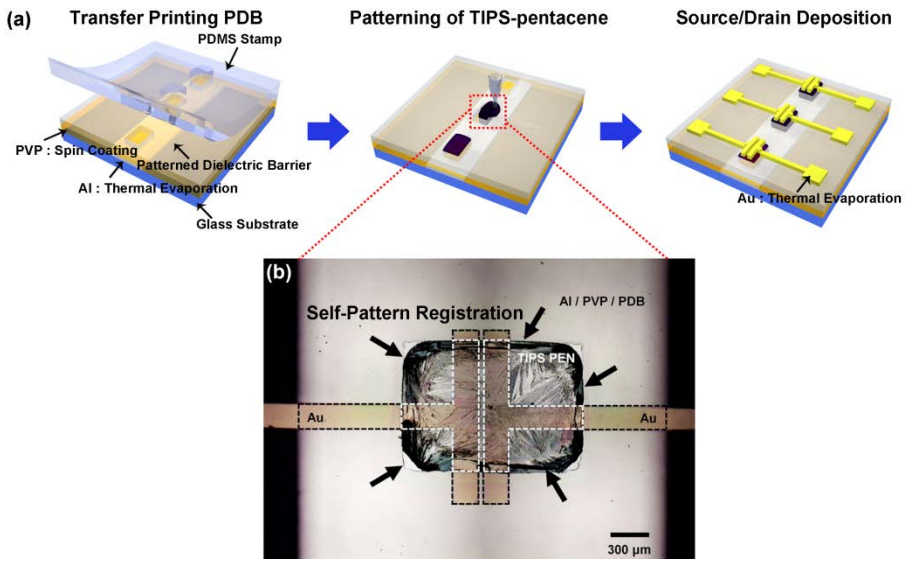

Figure 3.3. (a) The fabrication processes for the OFET with the PDB. (b) The microscopic image of the top-view of the fabricated OFET. The MIM and MISM regions are enclosed by black dashed lines and white dashed lines, respectively. The black arrows represent the pattern boundary of self-registration. (Ref. [64])

For the PDB, a hydrophobic fluorinated-polymer (Novec™ EGC-1700, 3M) dissolved in a fluorinated-solvent (Novec™ HFE-7100, 3M) was transfer-printed onto the substrate using the PDMS stamp with complimentary patterns of the organic semiconductor. Due to the low surface energy of the PDMS compared to that of the underlying gate insulator, the PDB on the PDMS stamp was easily transferred without any additional treatment such as pressure and temperature [65]. The physical properties of EGC-1700 are provided in Table 3.1. The organic semiconductor used in this study was 6,13-bis(triisopropylsilylethynyl) pentacene (TIPS-pentacene) of 1 wt.% dissolved in anisole. It should be noted that the solvent (anisole) is chemically inert to

the fluorinated-polymer layer and the PVP insulator. The TIPS-pentacene droplet was spontaneously confined only in the cavity formed by the PDB through selective wetting as clearly seen in Fig. 3.3(b). The TIPS-pentacene was thermally baked at 60°C for 30 min, and the source and drain electrodes were then prepared onto the TIPS-pentacene film by thermal evaporation of gold (Au) through a metal shadow mask to produce a channel with the length of 50 μm and the width of 1000 μm.

In Fig. 3.3(b), the MISM region (6.1×10^{-3} cm^2) was enclosed by white dashed lines and the MIM region (5.0×10^{-3} cm^2) by black dashed lines. These regions represent the overlap areas between two top (source and drain) electrodes and the bottom (gate) electrode in our OFET structure.

Table 3.1. The physical properties of EGC-1700

Properties	EGC-1700
Appearance	Clear, colorless to light-colored liquid solution
Specific Gravity at 25°C	1.5
Solvent	HFE-7100
Boiling Point of Solvent	61°C
Thermal Stability of Dry Film	Repellent to chlorinated silicone oil after 24 hrs at 175°C
Surface Energy of Dry Film	11-12 dynes/cm
Dielectric Constant at 25°C, 1 kHz	3.1
Coating Thickness (dip coated)	~1 μm
Dielectric Strength at 25°C	1.0 kV/25.4 μm
Refractive Index of Dry Film	1.38

3.3. Leakage Current Reduction

In this section, the current characteristics of the MISM structure and two MIM structures (one of which having only a gate insulator and the other having a fluorinated-polymer layer on a gate insulator) are first described to investigate how the PDB affects the leakage current in the OFET. Figure 3.4(a) shows the current density in the MISM capacitor (Al/PVP/TIPS-pentacene /Au) as a function of the applied voltage. The voltage applied to the Al electrode was swept from –5 V to 5 V while the Au electrode was grounded. The measured current density was less than 10^{-6} A/cm^2 in the range of the applied voltage up to 5 V, which contributes to the vertical current in the OFET.

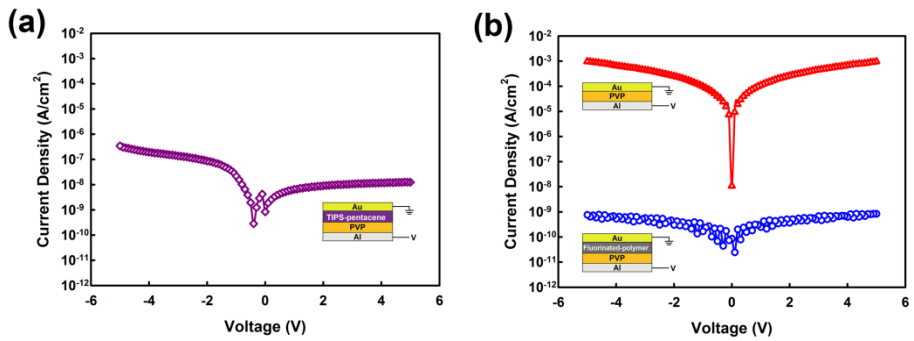

Figure 3.4. (a) The current density in the MISM capacitor of Al/PVP/TIPS-pentacene /Au and (b) the current densities in two MIM capacitors of Al/PVP/Au and Al/PVP/fluorinated-polymer/Au as a function of the applied voltage to the Al electrode. Open red triangles and open blue circles represent the current density of Al/PVP/Au and that of Al/PVP/fluorinated-polymer/Au, respectively. (Ref. [64])

Note that the magnitude is much smaller than the leakage current observed in typical OFETs [54, 55, 66], indicating that the current flow across the MISM region in the channel of the OFET is not the major contribution to the leakage current. The asymmetry in the leakage current with respect to zero applied voltage in Fig. 3.4(a) is attributed to the p-type nature of the TIPS-pentacene.

As shown in Fig. 3.4(b), the MIM with only the PVP layer of 100 nm thick as a gate insulator exhibited the current density of about 10^{-3} A/cm^2 at the applied voltage of 5 V while the MIM with an additional fluorinated-polymer PDB of 200 nm thick on the PVP layer showed the current density of about 10^{-9} A/cm^2 at the same applied voltage. In other words, the current density in the MIM structure was reduced by six orders of the magnitude by the introduction of a fluorinated-polymer layer as a dielectric barrier. Note that the symmetry in the leakage current with respect to zero applied voltage was fully preserved.

Figs. 3.5(a) and 3.5(b) show the capacitance characteristic of the PVP dielectric measured with an impedance analyzer (HP 4284A, Agilent Technologies) as a function of the frequency and the voltage, respectively. In Fig. 3.5(a), the value of measured capacitance is about 34.5 nF/cm^2 through overall frequency range, and is weakly dependent on the frequency near to 1 MHz, which implies that this insulator is applicable to the integrated circuits operated at high frequency. The capacitance with respect to the applied voltage is also constant so that the OFET can be operated at a low voltage as shown in Fig. 3.5(b).

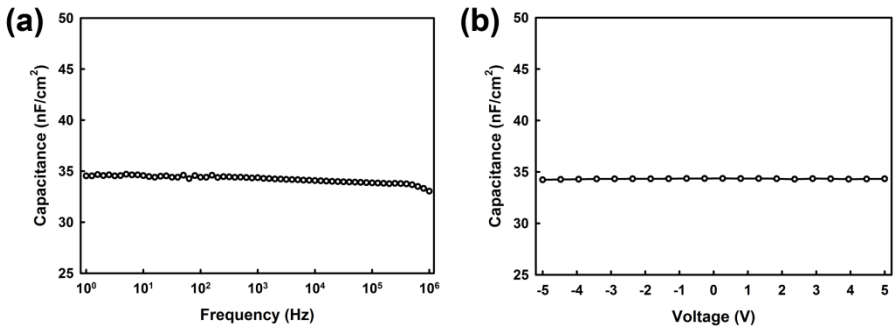

Figure 3.5. The capacitance characteristics of the PVP dielectric measured as a function of (a) the frequency and (b) the voltage, respectively.

Based on the above results, the role of the PDB on the current characteristics of the OFETs illustrated in Fig. 3.1(b) is examined. Two contributions to the leakage current depending on the current flow direction were independently measured as a function of the thickness (t) of the PDB. The PDB thickness was varied with the dip-coating rate and the concentration of the fluorinated-polymer solution. Figure 3.6 shows the lateral current measured at –5 V for the drain voltage and 0 V for the source and gate voltages together with the vertical current at –5 V for the gate voltage and 0 V for the source and drain voltages among three electrodes. Note that in this case, under the conditions that both the source and gate voltages are zero, the current flowing from the source to the drain through the organic semiconductor, not passing via the gate electrode, corresponds to the lateral current. The lateral current between the source electrode and the drain electrode remains fairly constant.

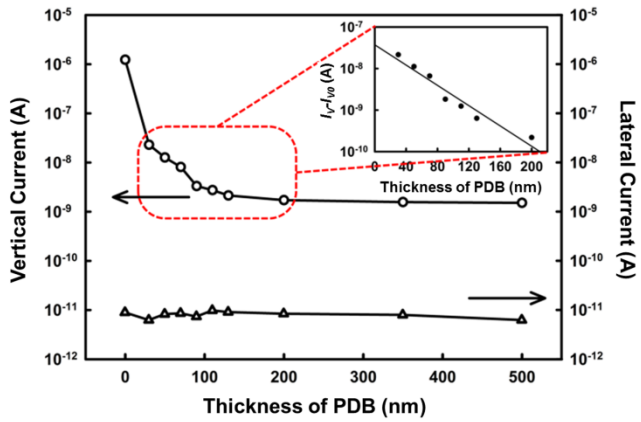

Figure 3.6. The vertical current (open circles) and the lateral current (open triangles) in OFET as a function of the thickness of the PDB. The inset shows the semi-logarithmic plot of ($I_V - I_{V0}$) as a function of t below 200 nm. (Ref. [64])

In contrast, the vertical current decays and eventually reaches a certain background value as the PDB thickness increases. As shown in the inset of Fig. 3.6, the decay behavior of the vertical current is analyzed in a form of

$$I_V = I_{V0} + I_{V1} \exp(-t/l) \tag{3.1}$$

where I_{V0} denotes the background value and I_{V1} represents the decaying part of the vertical current with the characteristic length l for the charge screening process. In fact, I_{V0} corresponds to the vertical current in the MISM and the characteristic length l depends on the material parameters as well as the interfacial properties of the PDB. Fitting the experimental data to the above form of the vertical current with the help of $I_{V0} = 1.50\times10^{-9}$ A taken at t = 500 nm where the vertical current vanishes in the MIM but remains in only the MISM, we have $I_{V1} = 3.73\times10^{-8}$ A and l = 35.7 nm. Converting the current density measured in the MISM at the voltage of –5 V in Fig. 3.4(a) into the

leakage current by the multiplication of the effective MISM area (6.1×10^{-3} cm^2) enclosed by white dashed lines in Fig. 3.3(b), the vertical current I_{Vs} was estimated to be 2.10×10^{-9} A. Note that this value of I_{Vs} is exactly on the same order of the magnitude of I_{V0}. Taking into account the variations of the thickness and the interfacial properties of the TIPS-pentacene between the two cases, the OFET in Fig. 3.3(b) and the MISM capacitor in Fig. 3.4(a), it is physically reasonable to claim that I_{Vs} is represented by I_{V0}.

3.4. Electrical characteristics

The electrical properties of the OFETs with the PDB were measured as a function of the applied voltage using a semiconductor parameter analyzer (HP 4155A, Agilent Technologies). The output characteristics of the OFETs without and with the PDB of 200 nm thick, measured with varying the gate voltage from 0 V to –5 V in a step of –1 V, are shown in Figs. 3.7(a) and 3.7(b), respectively. Clearly, in both types of the OFETs, a very well-defined saturation behavior of the drain current was obtained as a function of the drain voltage. Basically, no difference in the output characteristics between the two types of the OFETs was observed regardless of the presence of the PDB. This tells that the PDB does not influence the lateral charge transport along the TIPS-pentacene layer in contact with the PVP insulator.

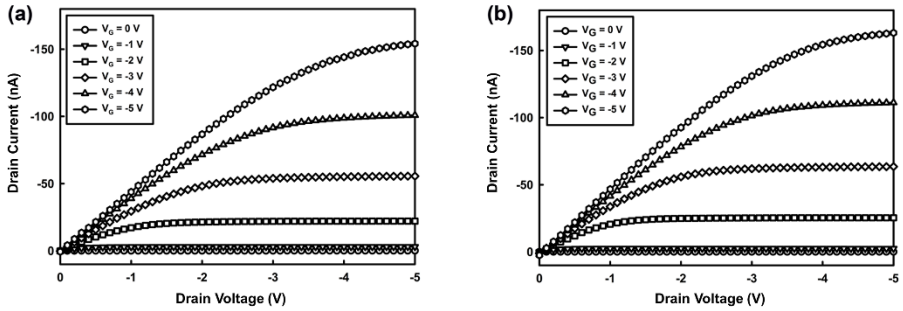

Figure 3.7. The output characteristics measured with varying the gate voltage from 0 V to –5 V in a step of –1 V for (a) the OFET without the PDB and (b) the OFET with the PDB (t = 200 nm). (Ref. [64])

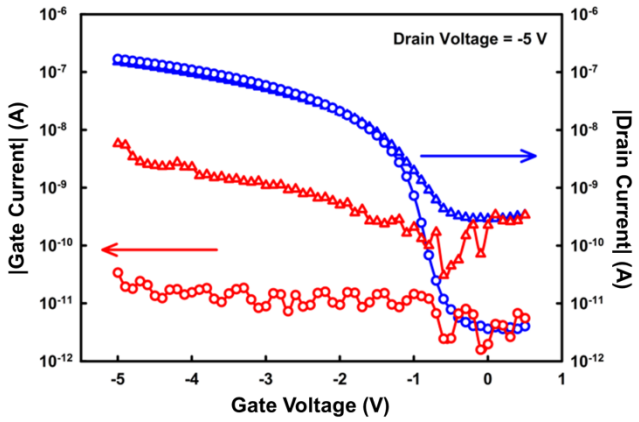

Figure 3.8. The drain current and the gate current at the drain voltage of –5 V as a function of gate voltage. Blue and red symbols represent the drain current and the gate current, respectively. Open circles and open triangles correspond to the OFET with the PDB and the OFET without the PDB, respectively. (Ref. [64])

Figure 3.8 shows both the drain current and the gate current for two types of the OFETs, one of which having no PDB and the other having the PDB of 200 nm thick, at the drain voltage of –5 V as a function of gate voltage. As shown in Fig. 3.8, extremely low gate current (< 10 pA) was obtained in the OFET with the PDB and it was two orders of the magnitude lower than the gate current in the OFET with no PDB. Moreover, the drain current on-off ratio was much increased from 5.2×10^{2} to 4.7×10^{4} in the low operation voltage regime. For both OFETs, the field-effect mobility in the saturation region, $(3.5\pm0.3)\times10^{-2}$ cm^2/Vs, was found to be nearly identical and the threshold voltage was about –0.5 V.

3.5. Summary

In summary, a novel architecture of the OFET, where the PDB was introduced to simultaneously achieve the leakage current reduction and the self-pattern registration of the soluble organic semiconductor, was demonstrated. The leakage current was reduced by two orders of the magnitude compared to that for a typical OFET with no PDB. The physical origin of the leakage current in the OFET was systematically analyzed in terms of the lateral and vertical contributions, one of which corresponds to the current flow along the organic semiconductor layer and the other to the current flow across the MIM as well as the MISM. The PDB is capable of effectively screening out the vertical charge flow and providing a cavity like a via-hole structure. Finally, the approach presented here would provide a basis for developing solution-processed integrated circuits that have low current leakage current and small operation voltages.

Chapter 4. Mobility Enhancement of Solution-Processed Organic Field-Effect Transistors

4.1. Introduction

The electrical properties of the device fabricated with an organic material greatly depend on the structural order of the organic semiconductor molecules. In the organic semiconductors with π-orbital between co-facially stacked molecules, the chain ordering is known to significantly increase the mobility as discussed in **Section 2.1** [1, 67]. In case of the solution-process, the solutes deposition of organic semiconductor is greatly dominated by solvent evaporation behavior depending on the solvent property such as the boiling point and the surface tension [68, 69], and the molecular order and orientation are dynamically developed during a drying process, unlike the vacuum-deposition techniques. Therefore, it should be emphasized that the controlling of solvent drying which is essential and mandatory process for solution-based organic device is significant to improve the electrical performance.

When the organic semiconductor films are prepared by a typical solvent drying method which evaporates the solvent by placing the sample substrate on a hot-plate fixed to the specific temperature, the solvent of a sessile drop on the substrate would randomly evaporate in radial directions from the perimeter to the center. This directly gives rise to the molecular domains showing disordered state. Recently, for soluble low-molecular organic

semiconductors such as TIPS-pentacene, the molecular order is induced by either dip coating [70], solution-shearing [71], or hollow pen writing [72]. The use of blended TIPS-pentacene with a photo-reactive polymer [73] is another method of producing the molecular order when the exposure of ultra-violet light is carried out during the solvent evaporation.

From the viewpoint of the interfacial interactions, the physicochemical modification of the gate insulator surface can be achieved using a hydrophobic layer for the improvement of the crystallinity in the soluble organic semiconductor [26, 74]. In this case, the hydrophobic layer is necessarily different from the gate insulator so that the dielectric properties of the gate insulator are inevitably altered. Note that the interfacial properties of an organic semiconductor solution in contact with the gate insulator are particularly important in solution-process since they play critical roles on the field-effect mobility [75], the current leakage [64], and the uniformity [76] of the organic semiconductor film in a fully dried state. Therefore, a new approach taking into account the fluidic and volatile nature of the organic semiconductor solution should be explored for the mobility enhancement without sacrificing other electrical properties of the OFET.

In this chapter, two viable methods of inducing the molecular order of TIPS-pentacene are demonstrated by controlling the solvent spreading and drying. First, the systematical studies how the temperature gradient variation affects the molecular alignment phenomenon in a solution-processed organic semiconductor film as well as the corresponding electrical performances are carried out during thermo-gradient assisted solvent evaporation [77]. Secondly,

a concept of the UT of an inkjet-printed polymer insulator is introduced to produce anisotropic spreading and drying of the TIPS-pentacene droplet and to spontaneously develop the ordered structures over relatively large area during the solvent evaporation. The formation of the ordered structures showing the optical anisotropy in the solution-processed TIPS-pentacene film leads directly to the enhancement of the field-effect mobility.

4.2. Molecular Order by Anisotropic Solvent Drying

4.2.1. Thermo-gradient-assisted solvent evaporation

In **Section 4.2**, the effect of the temperature gradient variation on alignment phenomenon in a solution-processed organic semiconductor film is systematically studied. The TIPS-pentacene-based OFETs were fabricated in a top contact and bottom gate structure, as schematically illustrated in Fig. 4.1. The indium-tin-oxide (ITO) layer on a glass substrate was patterned to act as a gate electrode. The ITO patterned substrates were then cleaned sequentially with acetone, isopropyl alcohol, and methyl alcohol in an ultrasonicator for 10 min each. At each cleaning step, the substrates were rinsed with DI water for 5 min in an ultrasonicator and purged with nitrogen gas. The PVP mixed with MMF (125 wt.% of PVP) in PGMEA in 10 wt.% was spin-coated on the cleaned substrates in 3000 rpm for 30 sec. to form a gate insulator.

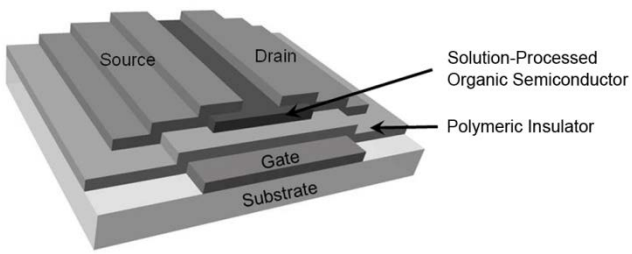

Figure 4.1. Schematic diagram of a solution-processed TIPS-pentacene-based OFET with a cross-linked PVP insulator. (Ref. [78])

The spin-coated PVP was baked at 100 °C for 10 min to remove the solvent, and subsequently annealed for 20 min at 200 °C to generate thermal cross-linking in the PVP layer. The thickness of the cross-linked PVP film was about 500 nm and the measured capacitance per unit area was 6.9 nF/cm^2. The capacitance was measured in a MIM structure using a semiconductor analyzer (4200-SCS, Keithley instruments, Inc.). For an organic semiconductor, TIPS-pentacene dissolved in anisole in 1.0 wt.%, was drop-casted onto the PVP gate insulator. For the reference samples, the drop-casted TIPS-pentacene was baked at a fixed temperature of 60°C on a hot-plate as shown in Fig. 4.2(a), which is a conventional method to evaporate the solvent. In order to apply the temperature gradient to the TIPS-pentacene droplet on a substrate (2 cm × 2 cm) during the solvent drying, one edge of a glass substrate was fixed at the room temperature (RT) on a thermal reservoir and the other edge was placed on a hot-plate as illustrated in Fig. 4.2(b). The temperature of a hot-plate was varied from 60°C to 120°C in a step of 30°C.

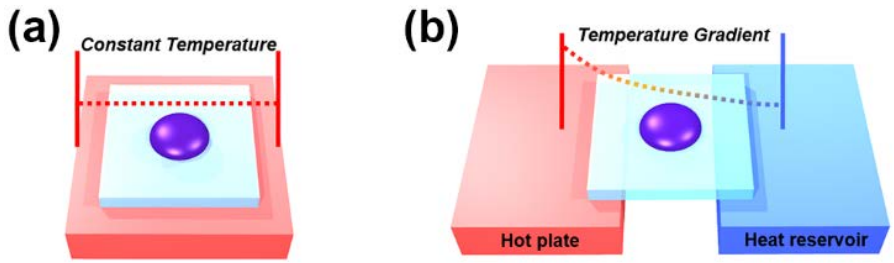

Figure 4.2. Conceptual illustration of (a) conventional solvent evaporation method where the temperature applied to a droplet is constant and (b) temperature gradient-assisted solvent evaporation method

In the thermo-gradient-assisted approach, the solvent is gradually evaporated along the direction of the temperature gradient from a high temperature region to a low temperature region in a TIPS-pentacene droplet, and the molecules are substantially aligned along the direction of the solvent evaporation as illustrated in Fig. 4.3 [77]. Note that the contact line of the drying droplet has to be pinned before the temperature gradient is applied so that the movement of droplet on the substrate by temperature gradient is prevented [79]. For source and drain electrodes, 80 nm-thick Au was thermally deposited onto the TIPS-pentacene film through a shadow mask under about 10^{-6} Torr. The channel length and width were 50 μm and 1 mm, respectively.

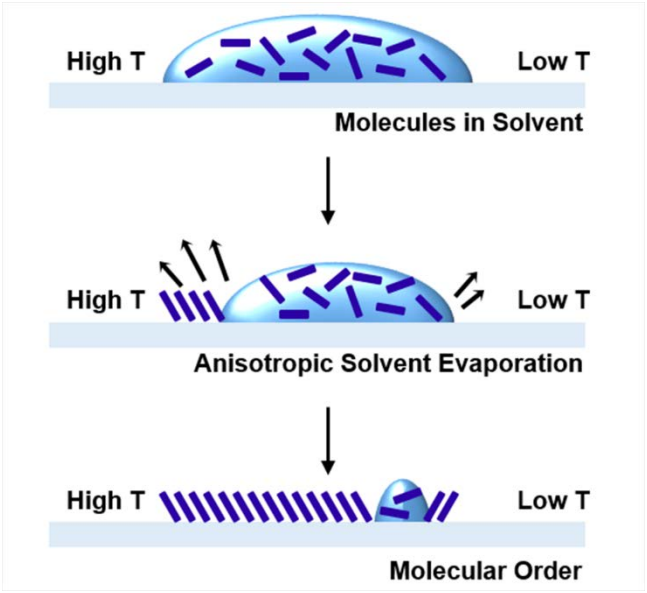

Figure 4.3. Schematic diagram showing the underlying concept behind the thermo-gradient-assisted solvent evaporation of a TIPS-pentacene droplet.

4.2.2. Molecular features

In this section, the molecular order in the TIPS-pentacene films as a function of the temperature gradient is examined. Figure 4.4(a) shows an optical microscopic image of the TIPS-pentacene film prepared by a conventional drying method (on a hot-plate fixed to 60°C), where the molecular domains are randomly distributed. The TIPS-pentacene films prepared by gradual solvent drying method are shown in Figs. 4.4(b), 4.4(c), and 4.4(d) as the optical microscopic images, where the temperature for one edge is RT fixed by the thermal reservoir and the temperature is varied to 60°C, 90°C, and 120°C for the other edge, respectively. It is clearly observed that the ordered molecular domains (needle shape) from high temperature region to low temperature region in the TIPS-pentacene films are spontaneously developed. It is attributed to the anisotropic solvent evaporation which is faster in a high temperature area than that in a low temperature area. Note that self-ordered TIPS-pentacene films are achieved only by thermal treatment without any additional help such as alignment layer. In a horizontal thermal gradient, the droplet on a substrate deviates from its original shape since the liquid surface tension is not uniform which is induced by the Marangoni effect [79]. This phenomenon results in a decrease of contact angle on the high-temperature region and an increase on the lower side. Therefore, the anisotropic solvent evaporation in the droplet is induced by obviously the temperature difference as well as the deviation of contact angle.

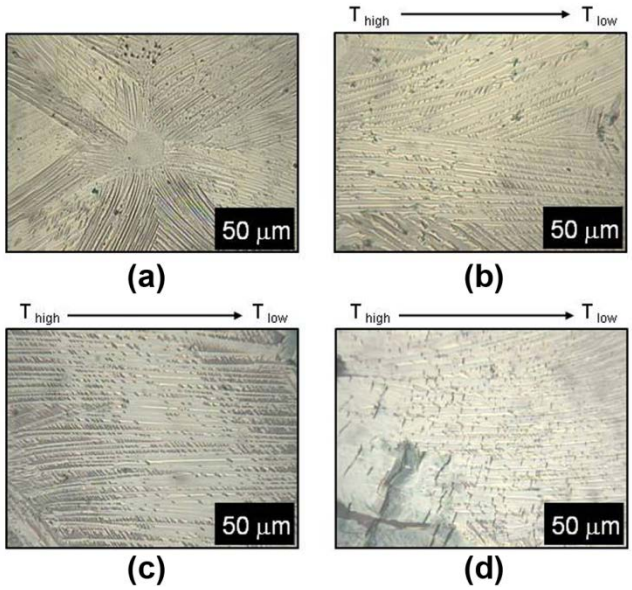

Figure 4.4. The optical microscopic images of the TIPS-pentacene films prepared by (a) the conventional method at 60°C and by the anisotropic solvent drying method at (b) RT-60°C, (c) RT-90°C, and (d) RT-120°C. (Ref. [78])

As the temperature of a hot-plate increases from 60°C to 90°C with remaining the heat reservoir at RT, it is found that TIPS-pentacene molecules tend to be more ordered and the molecular domains are more elongated as shown in Figs. 4.4(b) and F4.4(c), since the unidirectional alignment of TIPS-pentacene molecules would be efficiently induced due to larger difference of solvent evaporation rate between two edges. Note that the optimal temperature maximizing the molecular ordering can be differently determined depending on the kind of the solvent used to dissolve the organic semiconductor. Considering that the initial thermal cracks in the TIPS-pentacene film inevitably occurs at about 90°C [80], when the temperature on the hot-plate

further increases above 90°C, cracks begin to develop in the higher temperature region and propagate to the low temperature region with deteriorating the aligned features as shown in Figs. 4.4(c) and 4.4(d).

To more specifically elucidate the molecular order, X-ray diffraction (XRD) of TIPS-pentacene films was measured. Figure 4.5(a) exhibits the typical series of (00*l*) reflections of the TIPS-pentacene film generated at RT-90°C condition. This result shows the preferential orientation of the TIPS-pentacene molecules, and the sharp diffraction peaks indicate the formation of highly ordered domains [80, 81]. The XRD peak intensities as a function of the temperature for the (001) plane in the TIPS-pentacene films prepared by both methods are shown in Fig. 4.5(b). For the case of temperature-gradient, the (001) diffraction peak reaches a maximum at RT-90°C condition and then decreases again while the peak intensity for the conventional method case monotonically decreases as the temperature increases.

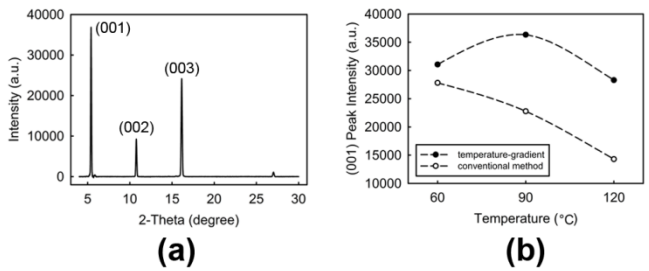

Figure 4.5. (a) Typical series of (00*l*) reflections of the XRD measured for the TIPS-pentacene film generated at RT-90°C condition. (b) The XRD peak intensities as a function of the temperature for the (001) plane in the TIPS-pentacene films prepared by either temperature-gradient or conventional method. (Ref. [78])

For the TIPS-pentacene film prepared by applying temperature-gradient, it is expected that the effective temperature was presumably not reached to 90°C and the effect of gradual evaporation of solvent was dominant on the structural orientation of TIPS-pentacene molecules at RT-90°C condition.

4.2.3. Electrical characteristics

Now, the effects of various conditions of the temperature gradient on the electrical performances are investigated. Figures 4.6(a) and 4.6(b) show the thickness of TIPS-pentacene film prepared by the conventional drying and the anisotropic solvent drying, respectively. Note that even though the TIPS-pentacene film prepared by anisotropic solvent drying shows the asymmetrical thickness gradient along the solvent evaporation direction, the thickness of channel area is almost same with that of conventional drying case (about 150 nm). Therefore, the electrical properties are essentially dependent on the molecular ordering features for both drying methods.

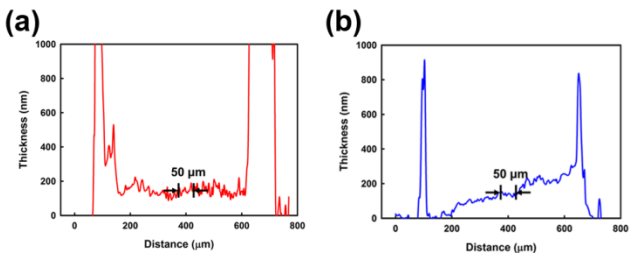

Figure 4.6. Thickness of TIPS-pentacene film prepared by (a) the conventional drying and (b) the anisotropic solvent drying.

The output curves of each OFET fabricated by either the conventional solvent drying or the anisotropic solvent drying are shown in Fig. 4.7. The magnitude of the saturated drain currents at a given drain and gate voltages of -50 V in the OFETs is -16.5 μA for the typical solvent drying case (Fig. 4.7(a)) and increases to -39.3 μA at 90°C (Fig. 4.7(c)) and then decreases to -20.1 μA (Fig. 4.7(d)) above 90°C with increasing the hot-plate temperature. Here, the output curves are deviated from ideal drain current-voltage characteristics in a linear regime when the anisotropic drying method is applied. This is attributed to the asymmetric TIPS pentacene film thickness since the larger thickness of the semiconductor causes the increase of effective contact resistance.

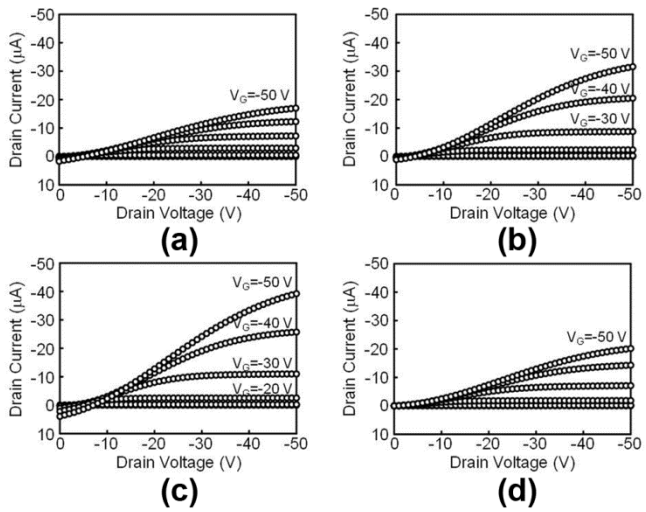

Figure 4.7. The output characteristic curves of four OFETs. The TIPS-pentacene film was prepared by (a) a conventional solvent drying method at 60°C and by the anisotropic solvent drying method at (b) RT-60°C, (c) RT-90°C, and (d) RT-120°C. The curves were obtained with varying the gate voltage from 0 V to -50 V in a step of -10 V. (Ref. [78])

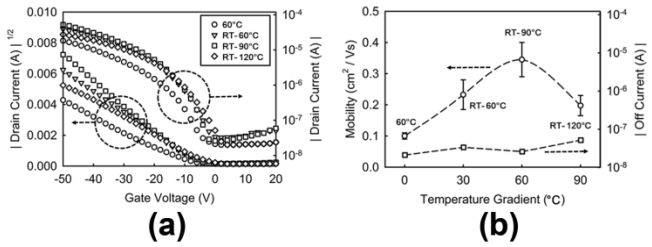

Figure 4.8. The transfer characteristic curves of four types of OFETs. Open circles, triangles, squares, and diamonds represent the conventional solvent drying case, anisotropic solvent drying case at RT-60°C, RT-90°C, and RT-120°C, respectively. The data at the drain voltage of -50V was used for obtaining the mobility of OFETs. (b) Magnitude of both the mobility and the off current in each OFET as a function of the temperature-gradient between a heat reservoir fixed at RT and a temperature variable hot-plate. Open circles and squares represent the mobility and the off current, respectively. (Ref. [78])

From the transfer characteristic curves as shown in Fig. 4.8(a), the mobility in the saturation region is theoretically extracted by Eq. (2.5). For all OFETs, V_{th} extracted from the square-root of I_D as a function of V_G was found to be nearly identical (-6±1 V). The mobility variation as a function of temperature gradient including a typical solvent drying case is shown in Fig. 4.8(b). The mobility in the OFET processed using a typical solvent drying method is 0.1 cm^2/Vs. For an anisotropic solvent drying case, the mobility increases up to about 0.4 cm^2/Vs at RT-90°C due to ordered TIPS-pentacene molecules. Note that the mobility was found to be increased by a factor of about four when the gradual solvent drying method is used. Above 90°C, the mobility decreases to 0.2 cm^2/Vs due to the appearance of thermal cracks. The

error bars represent standard deviations deduced from ten different samples. This result implies that the molecular order characteristics presented in Fig. 4.4 directly influence the charge transport property in an organic semiconductor. In addition, the magnitude of the off-current at the gate voltage of 0 V under applying the drain voltage of -50 V is found to be nearly same regardless of the conditions for evaporating the solvent in the TIPS-pentacene film. Note that the current on-off ratio is above 10^3 for all devices.

4.3. Topography-Guided Solvent Spreading and Drying

4.3.1. Unidirectional topography of inkjet-printed polymer dielectric

In contrast to the alignment of a liquid crystal, which is a highly viscous and non-volatile fluid, on a micro-grooved surface according to the elasticity argument [82], the structural arrangement of the TIPS-pentacene molecules is most likely achieved through anisotropic wetting, spreading, and drying along the UT on the gate insulator produced by inkjet printing. In **Section 4.3**, the development of the structural order of the TIPS-pentacene molecules is described in terms of the anisotropic wetting phenomenon together with the directional flow during the solvent evaporation along the UT. The construction of the UT of a polymer insulator by inkjet printing is schematically shown in Fig. 4.9. A series of the droplets of a polymer solution are printed in line such that the droplets are partially connected. As a basic element of the UT, a ridge structure with periodic arcs is naturally developed during the anisotropic solvent evaporation along the direction of inkjet printing. Note that the periodic arc boundary in the ridge is attributed to the coffee-ring effect [83-85] which is commonly observed in a liquid droplet containing dispersed solids during the drying process. The inset in Fig. 4.9 shows the optical microscopic image of a single droplet pattern of PVP on a glass substrate where the coffee-ring effect is clearly seen. The geometrical

factors such as the width (*w*) and the height (*h*) of the ridge depend primarily on the printing pitch (*p*) and the radius (*r*) of the droplet of the polymer solution. The center-to-center distance (*d*) between two adjacent ridges is simply given by the spatial interval in inkjet printing. A polymer dielectric material of PVP mixed with MMF (100 wt.% of PVP) in PGMEA in 5 wt.% was used for producing the gate insulator with the ridge structures by inkjet printing. Inkjet printing was performed using a piezoelectric printer (UJ200, Unijet Co.), equipped with a nozzle having the orifice diameter of 50 μm (MJ-AT, MicroFab), at the frequency of 1 kHz in a bipolar type wave form.

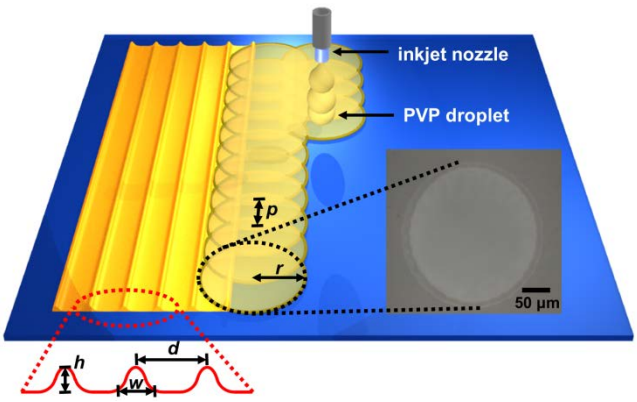

Figure 4.9. Schematic diagram showing the construction of UT of PVP on top of the uniform PVP insulator by inkjet printing. The radius of a single PVP droplet and the printing pitch are denoted by *r* and *p*, respectively. The width and the height of the ridge formed by a series of the droplets printed in line are *w* and *h*, respectively. The center-to-center distance between two adjacent ridges is *d*. The inset is the optical microscopic image of a single PVP droplet pattern showing the coffee-ring effect. (Ref. [86])

The ridge structures of PVP were constructed on the top of a uniform PVP layer which was prepared on a glass substrate by spin-coating. The substrate was maintained at 60°C during spin-coating and inkjet printing. For a single PVP droplet with the volume of 40 pL in solution, the average radius (r) on the uniform PVP layer was about 110 μm as shown in the inset of Fig. 4.9.

The optical microscopic image of the PVP ridges constructed on the uniform PVP layer by inkjet printing is shown in Fig. 4.10. From the geometrical profiles of the PVP ridge measured using a surface profiler (alpha step 500, KLA-Tencor), it was found that h = 350 nm, w = 30 μm, and d = 55 μm.

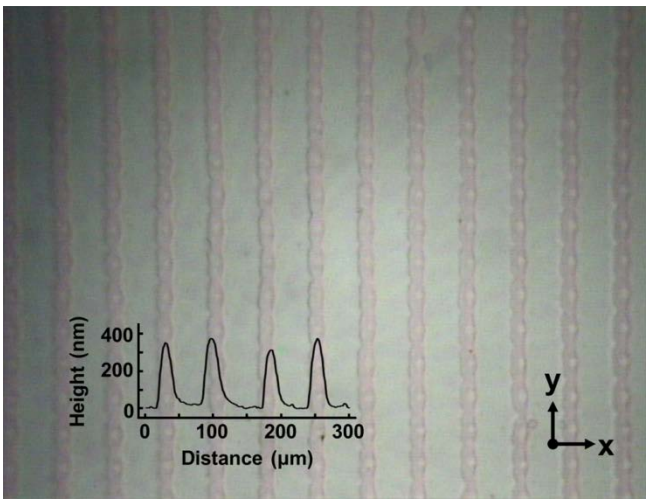

Figure 4.10. The optical microscopic image of PVP ridges constructed on the uniform PVP layer by inkjet printing and the geometrical profiles of several PVP ridges. The x-axis and y-axis are defined as the directions perpendicular and parallel to UT, respectively. (Ref. [86])

These parameters depend on the experimental conditions, such as the volume (or the radius) of the droplet, the printing pitch, the solvent evaporation rate, and the substrate temperature, together with the intrinsic properties of the substrate including the surface energy and the morphology. Note that the periodic ridges forming the UT were built up in the PVP-on-PVP configuration to eliminate any detrimental effect at an insulator-insulator interface.

First, the wetting behavior of DI water on two types of the PVP insulator surfaces, one of which is spatially uniform and the other has the UT, was examined. The *x*-axis and the *y*-axis represent the direction perpendicular to the ridge and the direction parallel to the ridge, respectively, as shown in Fig. 4.10. The contact angle of water on a uniform PVP surface was circularly symmetric ($\theta_s = 75°$) as shown in Fig. 4.11(a). For the UT on the uniform PVP, as seen from Figs. 4.11(b) and 4.11(c), the contact angle was $\theta_{\perp} = 81°$ along the *x*-axis while it was $\theta_{\parallel} = 70°$ along the y-axis according to the geometrical anisotropy of the UT. This is consistent with the anisotropic wetting phenomena of liquids on a large number of textured surfaces [87-90]. In Wenzel's model [29, 91, 92] for anisotropic wetting of a liquid on a textured surface, the relationship between the apparent angle θ_a and the intrinsic contact angle θ_{CA} on a smooth surface can be expressed as $\cos\theta_a = k\cos\theta_{CA}$ as given by Eq. (2.2). Moreover, it is well known that the geometrical anisotropy on the textured surface breaks the symmetry of the contact line at the liquid-solid boundary [88], indicating that the liquid tends to spread along the ridges but is restricted in the direction perpendicular to the ridges.

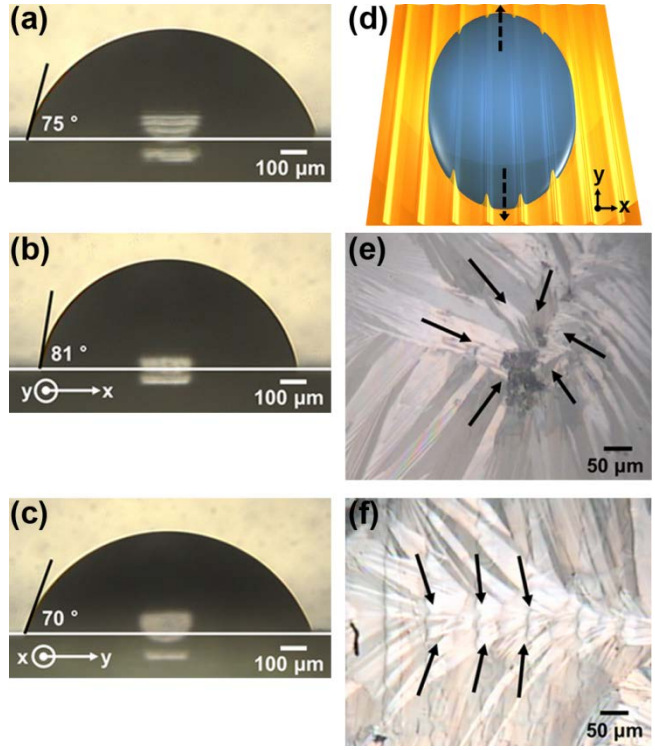

Figure 4.11. The contact angles of water on (a) the uniform PVP insulator prepared by spin-coating (θ_s), (b) on PVP insulator with the UT measured along the *y*-axis ($\theta_{\perp}$), and (c) on PVP insulator with UT measured along the *x*-axis ($\theta_{\parallel}$). (d) The schematic illustration of an elongated TIPS-pentacene droplet formed on PVP insulator with UT by anisotropic wetting. The black dashed arrows indicate the directions of preferential spreading of the droplet along the ridges. The optical microscopic images of the TIPS-pentacene films prepared (e) on a uniform PVP film and (f) on PVP with UT. The radial domains on the uniform PVP and the elongated, bilateral domains along UT of PVP are indicated by black solid arrows. (Ref. [86])

This means that the liquid droplet should be elongated along the ridge direction. In other words, using θ = 75°, k was about 1.3 for θ_a = 70° and

about 0.6 for θ_a = 81° in a first-order approximation where the interfacial interactions are ignored [88, 89]. Similarly, for the TIPS-pentacene solution, an elongated droplet is formed on the PVP insulator with the UT by anisotropic wetting as shown schematically in Fig. 4.11(d). The directional flow is then generated along the UT during the solvent evaporation, and the structural order of the TIPS-pentacene molecules is accordingly developed. In our study, a droplet of 1 μL of TIPS-pentacene dissolved in anisole in 1 wt.% was placed on the PVP insulator with the UT at RT and allowed for the solvent evaporation at 60℃ for 30 min. The optical microscopic image of the TIPS-pentacene film prepared on a uniform PVP film and that on the UT of the PVP are shown in Figs. 4.11(e) and 4.11(f), respectively. It is clear that in contrast to the random, radial domains (indicated by black arrows) observed on the uniform PVP insulator, the elongated, bilateral domains were developed along the UT of the PVP insulator as shown in Fig. 4.11(f).

4.3.2. Analysis of molecular alignment

In analyzing the structural order of the TIPS-pentacene molecules in terms of the optical anisotropy, the optical retardation measurements were carried out using a photoelastic modulator (PEM) (PEM90, Hinds Instruments), which has been commonly used for characterizing liquid crystals [93] and pentacene [94], as shown in Fig. 4.12(a). The PEM with a fused silica head was placed between two crossed polarizers that were oriented at ±45° with respect to the optic axis of the PEM head. A 633nm-

laser beam was incident normal to the TIPS-pentacene film sample. The signal fed into a lock-in amplifier (SR830, Stanford Research Systems) from a photodetector was monitored during rotation of the sample. Figure 4.12(b) shows the optical retardation values for the uniform PVP insulator (open circles) and those for the PVP insulator with the UT (filled circles) as a function of the azimuthal rotation angle (φ). In both cases, the PVP insulators were optically isotropic irrespective of the presence of the UT. However, when the TIPS-pentacene film was crystallized on the PVP insulator after the solvent evaporation, the optical anisotropy resulted from the molecular order was observed as shown in Figs. 4.12(c) and 4.12(d). Different color curves represent five different samples.

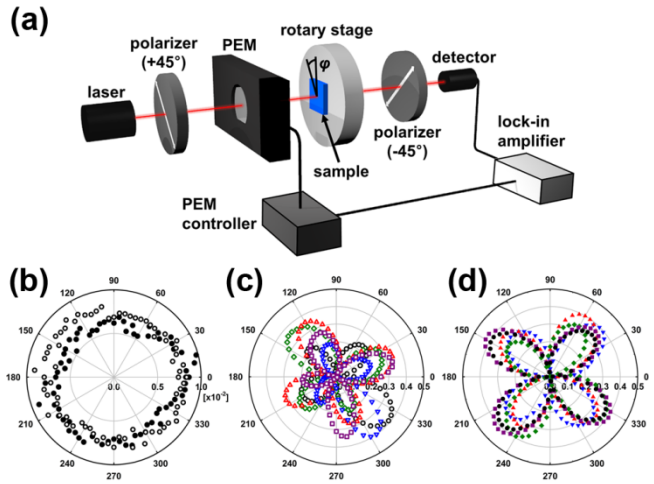

Figure 4.12. (a) The experimental setup for the measurements of the optical anisotropy. The optical retardation values for (b) the uniform PVP (open circles) and PVP with UT (filled circles), (c) TIPS-pentacene film on the uniform PVP, and (d) TIPS-pentacene film on PVP with UT. (Ref. [86])

For the uniform PVP case, the magnitude of the optical anisotropy and the direction of the optic axis of the TIPS-pentacene film were quite different from sample to sample as shown in Fig. 4.12(c) while for the UT case, the optic axis was very well-defined along the UT and the magnitude was fairly constant as shown in Fig. 4.12(d). The average value of the retardation maxima of the five samples was found to be 0.279±0.072 for the uniform PVP case and 0.366±0.037 for the UT case. This indicates that the UT of the PVP insulator indeed increases the degree of the molecular order and the crystallinity of the TIPS-pentacene film by the directional flow during the solvent evaporation.

4.3.3. Electrical characteristics

Now, the electrical properties of the TIPS-pentacene OFETs with two types the PVP insulators, one with no UT and the other with the UT, are investigated in a bottom-gate, top-contact configuration as illustrated in Fig. 4.13. The gate electrode was prepared using 120 nm-thick-ITO, and the source and drain electrodes were gold (60 nm). The channel was produced along a direction either perpendicular or parallel to the UT of the PVP insulator. The channel length and the channel width were 50 μm and 1000 μm, respectively, defined by a metal shadow mask during thermal evaporation. For the PVP insulator with the UT, there are two different channel geometries in the directions perpendicular and parallel to the UT.

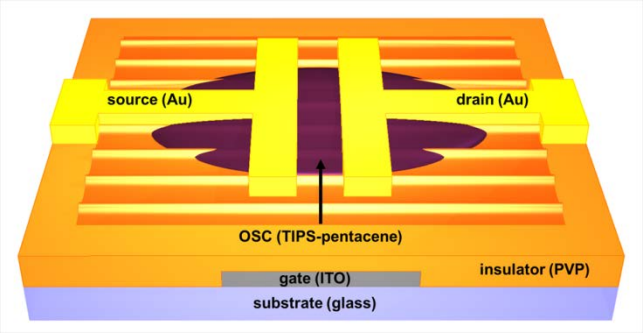

Figure 4.13. Schematic diagram showing a TIPS-pentacene OFET on PVP insulator with UT in a bottom-gate, top-contact configuration. (Ref. [86])

The electrical characteristics were measured using a semiconductor parameter analyzer (HP 4155A, Agilent Technologies). Figure 4.14(a) shows the output characteristics of three OFETs, the first on the uniform PVP, the second on the UT perpendicular to the channel, and the third on the UT parallel to the channel, as a function of drain voltage for the gate voltages of –10 V, –30 V, and –50 V. The difference in the saturated drain current between the uniform PVP case and the UT case along the channel increases with increasing the drain voltage for given gate voltage. Relative to the uniform PVP case, the saturated drain current for the channel parallel to the UT was increased by more than two-fold but that for the channel perpendicular to the UT was decreased by a factor of about one half. The transfer characteristics for the three cases were shown as a function of the gate voltage at the drain voltage of –50 V in Fig. 4.14(b). The insets are the optical microscopic images of the channel regions for the three cases.

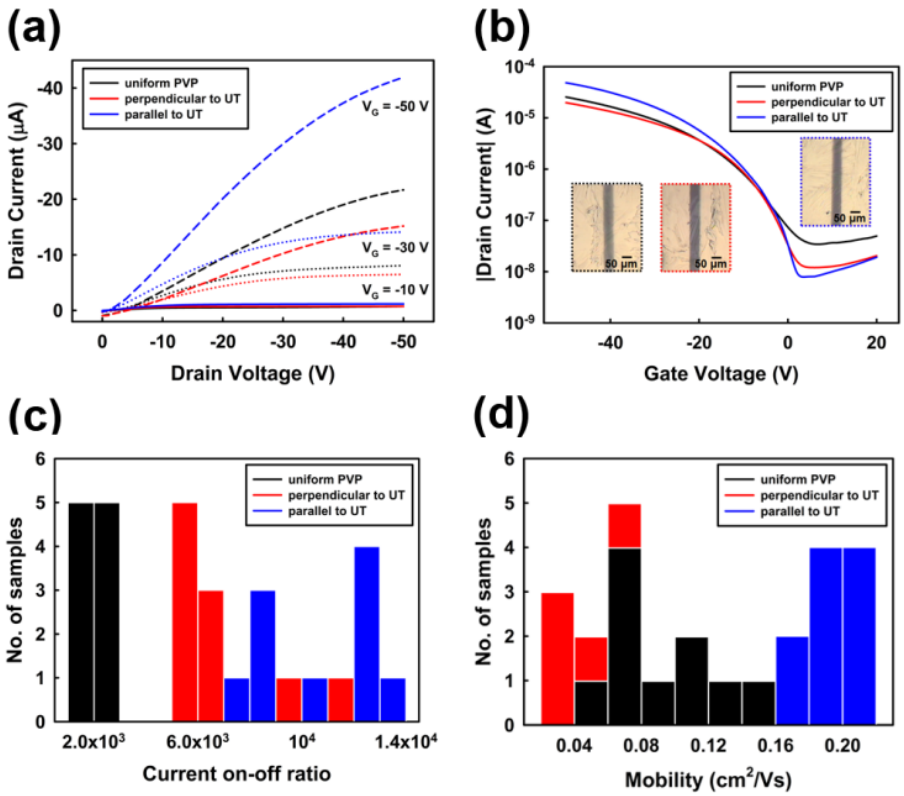

Figure 4.14. (a) The output characteristics as a function of drain voltage for the gate voltages of –10 V (solid lines), –30 V (dotted lines), and –50 V (dashed lines) for three OFETs on the uniform PVP (black lines), on PVP with UT perpendicular to the channel (red lines), and on PVP with UT parallel to the channel (blue lines). (b) The transfer curves for the three cases as a function of the gate voltage at the drain voltage of –50 V. The insets are the optical microscopic images of the channel regions for the three cases. Histograms showing the distribution of (c) the current on-off ratio values and (d) that of the mobility values for the three cases. (Ref. [86])

It is clear that for the channel parallel to the UT, the uniformity of the TIPS-pentacene film was significantly improved, and the magnitude of the drain

current was much enhanced. Another point is that the UT results in the reduction of the off-current irrespective of the channel geometry as shown in Fig. 4.14(b). This may be attributed to the role of the UT to screen out the vertical charge flow generated from the gate electrode, which is consistent with previous work discussed in **Chapter 3** [64]. Thus, the on/off current ratio was substantially increased (about 10^4) for the case of UT parallel to the channel. Figure 4.14(c) shows the distribution of the on/off current ratio values of ten OFETs fabricated in different batches for the three cases.

From the transfer characteristic curves in Fig. 4.14(b), the field-effect mobility of each OFET can be extracted from the slope of the square root of the saturated I_D as a function of V_G as given by Eq. (2.5). The capacitance in a MIM structure as a function of the voltage was measured using a semiconductor analyzer (4200-SCS, Keithley instruments, Inc.) The measured values of C_i for the uniform PVP and the PVP with the UT were about 4.9 nF/cm^2 and 3.9 nF/cm^2, respectively. The average mobility values measured for the three cases, i.e., the channel on the uniform PVP (μ_s), the channel parallel to the UT on the PVP ($\mu_{\parallel}$), and the channel perpendicular to the UT on the PVP ($\mu_{\perp}$), over ten different samples were μ_s = 0.090±0.032, $\mu_{\parallel}$ = 0.202±0.012, and $\mu_{\perp}$ = 0.052±0.014 cm^2/Vs. The mobility was enhanced by 2.2 along the direction of the UT but decreased by 0.6 in the direction perpendicular to the UT. The distribution of the mobility values for the three cases is shown in Fig. 4.14(d). The electrical performances for three structures were summarized in Table 4.1.

Table 4.1. The electrical performances (mobility, on/off current ratio, V_{th}) for three structures

Structure	Mobility (cm^2/Vs)			On/Off Ratio	V_{th} (V)
	Range	Mean	Standard deviation		
uniform PVP	0.05~0.15	0.09	0.032	~10^3	
parallel to the UT	0.19~0.22	0.202	0.012	~10^4	-6 ± 1
perpendicular to the UT	0.03~0.065	0.052	0.014	~10^4	

4.4. Summary

In this chapter, the concepts of controlling the solvent spreading and drying were introduced for inducing the molecular order of solution-processed TIPS-pentacene. First, the trade-off relationship between the molecular order and cracks by controlling the temperature gradient and corresponding electrical properties in TIPS-pentacene OFETs with a polymer insulator were presented. As increasing the temperature gradient, the mobility increases and reaches about 0.4 cm^2/Vs, which is attributed to ordered molecules, and then decreases due to cracks generated in the TIPS-pentacene film. Secondly, the concept of UT for the enhancement of the field-effect mobility of solution-processed TIPS-pentacene on an inkjet-printed polymer insulator was demonstrated. The underlying mechanism for the ordered structures of TIPS-pentacene arises from the anisotropic wetting, spreading, and drying phenomenon guided by the UT during the solvent evaporation. The mobility of the UT-dictated TIPS-pentacene film was found to increase by more than two compared to that of the isotropic case. Moreover, the off-current was much reduced and the current on-off ratio was significantly increased by screening out the vertical charge flow generated from the gate electrode. Both anisotropic solvent drying method assisted by temperature gradient and UT-based approach will serve as a firm basis for developing diverse solution-processed organic devices including the OFETs and inverters

Chapter 5. Quasi-Surface Emissive Organic Light-Emitting Transistors

5.1. Introduction

Recently, rapid progress in organic electronics and photonics [95, 96] has led to the advancement of OLETs where the functionality of electrical switching and the capability of light generation are integrated in a single building block [4, 5, 97]. In addition to the intrinsic switching function, the OLET exhibits, in principle, higher quantum efficiency and a larger aperture ratio than an organic light-emitting diode [4, 6]. However, except for a few cases of carbon nanotube (CNT)-based VOLETs [41, 46], most of the OLETs have been constructed in lateral source-drain geometries and have shown line- or band-type emission characteristics [8, 11, 98-101] since the effective recombination zone for holes and electrons is limited within a hundred nanometer range between the source electrode and the drain electrode [4] as discussed in **Sections 1.3** and **2.5**. Thus, toward improving the device performance and extending the light emission area, a number of approaches such as multilayer structures [6, 102], modified electrodes [103-105], and p-i-n [106] or metal-insulator-semiconductor types [40, 107] have been suggested to effectively control the charge injection, the charge transport, and the charge carrier recombination throughout the entire device. Despite good material properties, the CNT-based vertical field-effect transistors [41, 43, 46] may

suffer from the uniformity as well as the long-term stability resulting from the random distribution as well as the poor connectivity of the CNTs used for the source electrode. Particularly, the interface between the CNT source electrode in contact with an adjacent layer, which is either an active layer of an organic semiconductor or an additional charge transport layer, becomes inevitably irregular and exhibits a wide range of the landscape of charge traps. Therefore, in a vertical architecture, the alternative is to introduce a source electrode with periodic vacancies instead of the CNTs. For example, the use of perforated electrodes [44, 108] and interdigitated electrodes [45] was found to provide a useful way of producing short channel length devices. In this case, the electric field should be precisely controlled through the vacancies of the source electrode from the gate electrode.

In this chapter, quasi-surface emissive VOLET with the help of a network source electrode of closed topology having periodic apertures of various sizes is demonstrated. An optical methodology of characterizing the apparent carrier recombination zone for light emission on a macroscopic level is also developed.

5.2. Vertical Structure with Network Source Electrode

5.2.1. Structure and fabrication

The cross-sectional schematic of VOLET is illustrated in Fig. 5.1. The basic operating mechanism and transistor performance of VOFETs have been discussed in terms of the potential barrier at the interface between the source electrode and the organic semiconductor with respect to the gate voltage [42, 44]. After the charge injection controlled by gate bias, it can be considered that the charge transport occurs in two steps, one of which is the lateral charge transport (q_L) in the plane of the organic semiconductor layer in a single aperture and the other is the vertical charge transport (q_V) out of the plane of the organic semiconductor into the emission layer through the vacancy (or aperture) of the source electrode as depicted in Fig. 5.1.

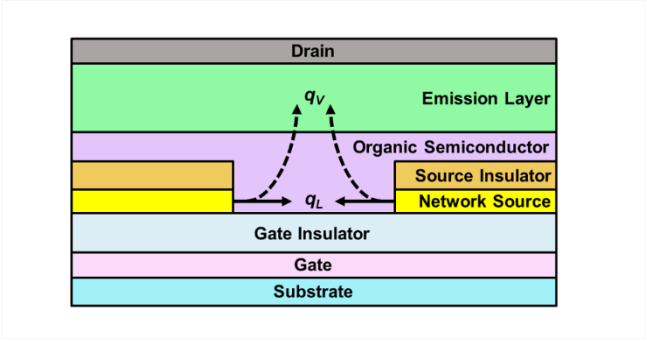

Figure 5.1. Cross-sectional view of our VOLET with a network source electrode having periodic apertures. The lateral charge transport (q_L) and the vertical charge transport (q_V) are depicted as solid and dashed arrows, respectively.

Here, q_V is directly involved in the charge recombination process, and can be approximately described using the space-charge limited current theory under an electric field between the drain and the source electrodes [44]. In case of q_L, it is primarily related to the actual emission area, and thus it is crucial to maximize the overlapped region of q_L for expanding the emission area in an entire device. Based on the above physical principles, the VOLET with a network source electrode was fabricated as illustrated in Fig. 5.2. First, glass substrates pre-patterned with the gate electrode (70 nm of TIO) were cleaned in an ultra-sonication bath using acetone, isopropyl alcohol, methanol, and DI water in sequence. As a gate insulator, 300 nm thick of silicon dioxide (SiO_2) was prepared by plasma-enhanced chemical vapor deposition and then PVP mixed with MMF (100 wt.% of PVP) in PGMEA in 2 wt.%, was coated at the spinning rate of 3000 rpm for 30 sec. The PVP film was soft-baked at 100°C for 10 min to remove the residual solvent and was thermally cross-linked at 200°C for 30 min.

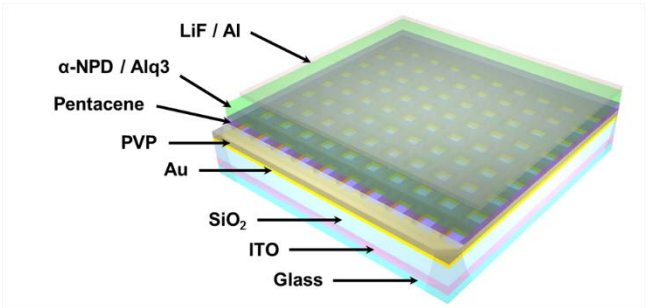

Figure 5.2. Illustration of our VOLET architecture with a network source electrode and the stacked layers of functional materials.

Figure 5.3 describes the fabrication procedure of the network source electrode. First, 15 nm thick of gold (Au) was deposited by thermal evaporation under about 10^{-6} Torr, followed by the preparation of the source insulator from a solution of the PVP in 10 wt.%. For the source insulator, the PVP solution was spin-coated and baked under the same conditions for the gate insulator described above. The PVP source insulator was patterned by conventional photolithography and dry-etching using a positive photoresist (PR) (AZ 5214, AZ electronic materials). After removal of the PR, the network source electrode having periodic apertures was generated by wet-etching using Au etchant (TFA, Transene) with the patterned PVP film being used as a mask.

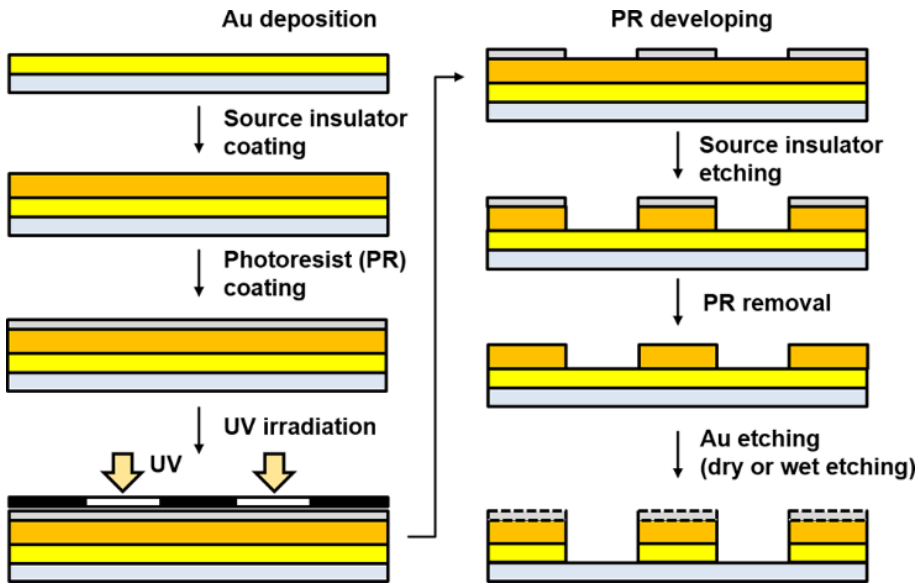

Figure 5.3. Fabrication procedure of the network source electrode by conventional photolithography and the dry (or wet) etching

Then, a pentacene film (100 nm), p-type organic semiconducting layer, was deposited by thermal evaporation at the rate of 0.1 nm/s under about 10^{-7} Torr. For the emitting part consisting of a hole transport layer and an emission layer, N,N'-di(1-naphthyl)-N,N'-diphenylbenzidine (α-NPD) (50 nm), tri-(8-hydroxyquinoline)aluminum (Alq_3) (50 nm), and the drain electrode of LiF/Al (0.5 nm/60 nm) were deposited on the pentacene layer in sequence.

5.2.2. Network source electrode

Figure 5.4 shows the microscopic images of three network source electrodes, having different sizes of the apertures, where the cross-linked PVP layers were prepared. One side of each square aperture (W_a) and the separation (W_e) between two adjacent apertures were set to be equal. The apertures of 20, 10, and 5 μm in size were shown in Figs. 5.4(a), 5.4(b), and 5.4(c), respectively.

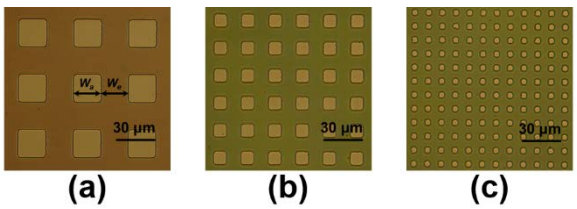

Figure 5.4. Microscopic images of three network source electrodes, having different sizes of the apertures, covered with the PVP layers. The size of each aperture and the separation between two adjacent apertures were denoted by W_a and W_e, respectively. The value of $W_a = W_e$ was varied to be (a) 20 μm, (b) 10 μm, and (c) 5 μm.

For small apertures, their shapes were much rounded and became even close to circles due to the patterning resolution in this study. For given organic semiconductor (pentacene) and emission material (Alq_3), the aperture size is a critical factor for achieving the light emission covering the whole aperture area. More specifically, the aperture size in relative to the characteristic length for the charge carrier recombination (or the length scale of the recombination zone) plays an essential role on whether the apparent emission occurs within the entire region of the aperture or not. In short, simply taking the characteristic length for the charge recombination as $W_a/2$, the emission area becomes W_a^2, meaning that the quasi-surface emission over the whole aperture is expected.

5.3. Quasi-Surface Light Emission

The light emission characteristics for three types of the VOLETs with three different aperture sizes of 20, 10, and 5 μm were first examined. Figures 5.5(a)-5.5(c) show the microscopic images for the light emission from the three VOLETs, taken with an optical microscope (Eclipse E600, Nikon), at the drain voltage of –10 V and the gate voltage of –10 V under zero source voltage. For the aperture of 20 μm, the light emission occurs only in the vicinity of the edges as shown in Fig. 5.5(a). As clearly seen in Figs. 5.5(b) and 5.5(c), the light emission becomes to cover nearly the entire area of the aperture with decreasing the aperture size.

In characterizing the spatial distribution of the light emission, the intensity profiles along the yellow line across a single aperture were measured and analyzed using two emission curves as shown in Fig. 5.5(d). Here, an image processing software (Image J, National Institute of Health) was used for the analysis. For the case of 5 μm, the apparent intensity across the aperture remains fairly constant owing to the overlap of two curves in the middle of the aperture. In contrast, for the case of 20 μm, two intensity curves were far separated from one another. This indicates that the closed topology (totally different from the interdigitated geometry) of the source electrode plays a critical role on extending the carrier recombination zone so as to achieve the quasi-surface emission in the OLET with the network source electrode. From two intensity curves separated from one another by extrapolation as shown in Fig. 5.5(d), the full width at half maximum (FWHM)

was estimated to be about 3.9±0.5 μm which is somewhat smaller than the aperture size of 5 μm. The FWHM is indirectly related to q_L in terms of the carrier mobility of the organic semiconductor, the charge injection barrier at the interface with the source electrode, and the geometrical factors such as the device architecture.

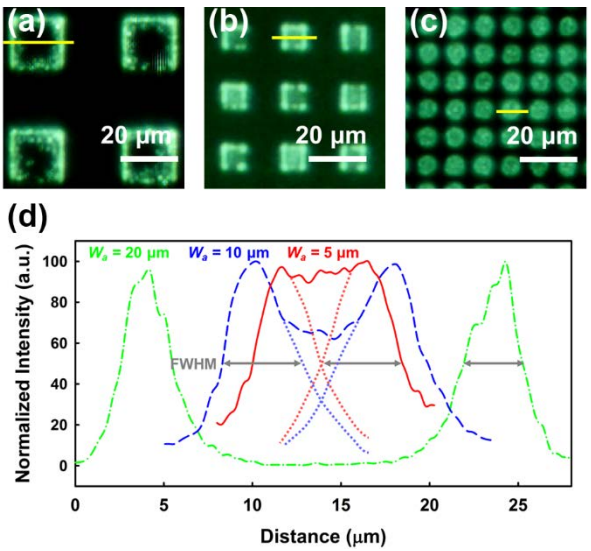

Figure 5.5. Microscopic images for the light emission through the apertures of the network source electrode in three VOLETs with different values of (a) W_a = 20 μm, (b) W_a = 10 μm, and (c) W_a = 5 μm at the drain voltage of –10 V and the gate voltage of –10 V under zero source voltage. (d) Intensity profiles along the yellow line across a single aperture for each OLET given in (a)-(c). Green, blue, and red colors represent W_a = 20, 10, and 5 μm, respectively. In each case, the FWHM (depicted by the gray arrow) was estimated from two intensity curves separated from one another by extrapolation.

5.4. Control of Luminance by Gate Voltage

We now describe the gate voltage-dependent luminance of our VOLET with the aperture size of W_a = 5 μm in the network source electrode. Figures 5.6(a)-5.6(c) represent the light emission features through 6 × 6 apertures in the source electrode at the gate voltage of –50 V, 0 V, and +50 V for fixed drain voltage of –10 V, respectively. From Fig. 5.6(b), it was found that our VOLET was in "the normally ON state" at the zero gate voltage, meaning that the charges were partially injected by the electric field between the drain electrode and the source electrode. This is because the potential barrier (about 0.5 eV), representing the difference in the energy level between the highest occupied molecular orbital of pentacene and the work function of Au, is not high enough to block the charge injection [16, 44, 109]. This potential barrier can be reduced by the application of a negative bias at the gate electrode so that more charges can be injected and recombined to enhance the light emission as clearly seen in Fig. 5.6(a).

Under a positive bias at the gate electrode, the charge injection becomes suppressed due to the increase of the effective potential barrier and thus the VOLET is switched off as shown in Fig. 5.6(c). Although the light emission of our VOLET was not uniform in aperture by aperture, it is evident that the experimental results fully support the validity of our device concept.

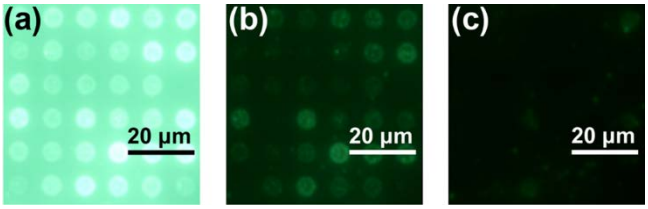

Figure 5.6. Light emission features through 6 × 6 apertures of W_a = 5 μm in the source electrode at the gate voltage of (a) –50 V, (b) 0 V, and (c) +50 V at the drain voltage of –10 V.

Figures 5.7(a) and 5.7(b) show the electroluminescence (EL) spectra and the color location with the values of x = 0.313 and y = 0.555 on the CIE 1931 color space chromaticity diagram, respectively. In Fig. 5.7(a), the EL spectra is slightly deviated around the wavelength of 600 nm from the smooth curve which is generally observed in normal OLED structure. This might be attributed to the light absorption while the light generated in the emission layer of Alq_3 travels through the organic semiconductor, the gate dielectric layer, and the glass substrate to be observed. However, a peak of EL spectra at about 525 nm is accordant with the previous literature [110].

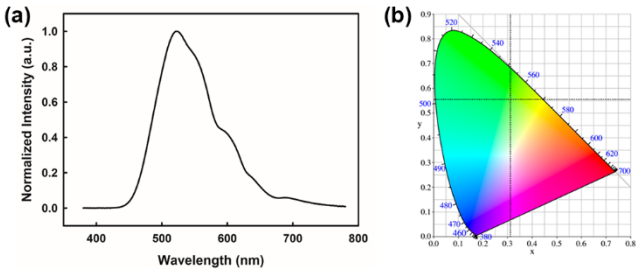

Figure 5.7. (a) Electroluminescence (EL) spectra of the emitted light (b) Color location (x = 0.313 and y = 0.555) on the CIE 1931 color space chromaticity diagram.

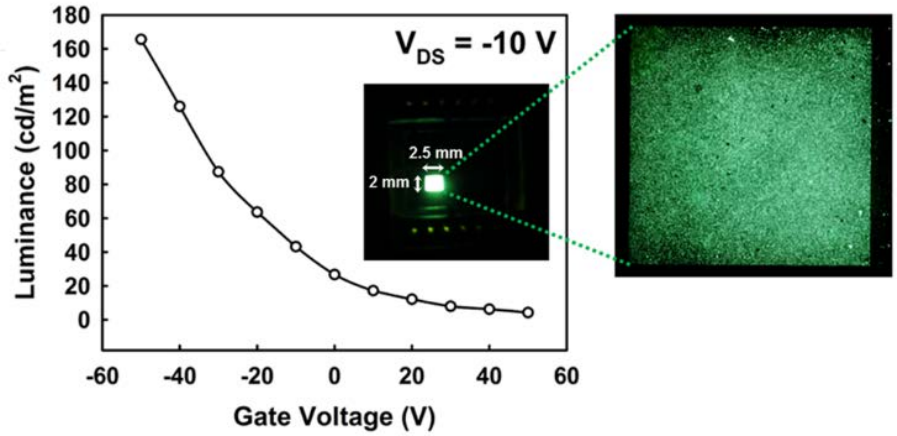

Figure 5.8. Luminance as a function of the gate voltage. The inset shows a photograph together with a zoom-in microscopic image for the light emission from the OLET (2.5 mm × 2 mm in size) with 50,000 apertures in the source electrode at the gate voltage of –50 V and the drain voltage of –10 V.

Figure 5.8 show the light emission characteristics curve of the luminance as a function of the gate voltage at the drain voltage of –10 V. A spectrometer (CS-2000, Konica Minolta) and a source meter (2636A, Keithley instruments, Inc.) were used to measure the luminance modulation by varying the applied voltage. The inset shows a photograph together with a zoom-in microscopic image for the light emission from a prototype OLET panel (2.5 mm × 2 mm in size) with 50,000 apertures in the source electrode at the gate voltage of –50 V for fixed drain voltage of –10 V. The luminance was measured to be about 170 cd/m^2 and the contrast ratio was about 40. These values are still far behind those for practical applications such as emissive displays. However, the optoelectronic performance might be much improved through the

optimization of the materials as well as the geometric parameters in analogy to the CNT-based transistors and OLETs [43, 46]. It should be emphasized that this VOLET provides indeed the light emission in a quasi-surface manner and the gate voltage-dependent luminance as observed from a prototype panel of 2.5 mm × 2 mm in size.

5.5. Summary

In summary, a new type of the VOLET showing the quasi-surface emission with the help of a network source electrode of closed topology was constructed. In contrast to the interdigitated geometry, the closed topology was found to allow the charge transport and the carrier recombination process in 2-dimension, extended from a bilateral direction, so that the quasi-surface emission of light was produced. The results indicate that the light emission area depends on the relative size of the aperture in the network electrode to the characteristic length scale for the charge carrier recombination. It was found that the luminance was well-controlled by the gate voltage. Although the improvement of the device performance through tailoring the materials and engineering the interfaces among different layers remains to be made, this approach to the surface emission-type VOLET serves as a new platform for developing advanced optoelectronic devices as well as next generation displays.

Chapter 6. Concluding Remarks

In this thesis, functional layer-by-layer engineering approaches were demonstrated in the scientific and technological viewpoints towards the development of advanced OFETs and OLETs. Specifically, leakage current reduction and mobility enhancement of solution-processed OFETs and VOLET showing the quasi-surface emission were studied within the framework of the interfacial modification and the device architecture construction. During the solution-process for fabricating OFETs, since the spreading and the drying of a liquid on a solid surface are essentially involved, engineering of the solid/liquid interfaces and understanding of the wetting properties of a liquid are of great relevance for controlling thermodynamic behaviors. In addition, a novel class of architecture incorporated with engineering of the multi-layers provides a wide range of opportunities for developing the advanced functional organic electronic devices such as VOLET.

First, a viable method of employing a PDB of hydrophobic polymer was demonstrated in order to achieve the leakage current reduction and the self-pattern registration of the soluble organic semiconductor simultaneously in the OFETs. The PDB is capable of effectively screening out the vertical charge flow and providing a cavity like a via-hole structure. The physical origin of the leakage current in the OFET was systematically analyzed in terms of the lateral and vertical contributions, one of which corresponds to the

current flow along the organic semiconductor layer and the other to the current flow across the MIM as well as the MISM.

Next**,** concepts of inducing the molecular order of solution-processed organic semiconductor for mobility enhancement were introduced. Solvent spreading and drying behaviors were controlled by employing either the temperature gradient method or UT of an inkjet-printed polymer insulator. In TIPS-pentacene OFETs with a polymer insulator, the trade-off relationship between the molecular order and cracks depending on the degree of temperature gradient was presented. In addition, the concept of UT for the enhancement of the field-effect mobility of solution-processed TIPS-pentacene on an inkjet-printed polymer insulator was also demonstrated. The underlying mechanism for the ordered structures of TIPS-pentacene arises from the anisotropic wetting, spreading, and drying phenomenon guided by the UT during the solvent evaporation. The elongated micro-structures of an inkjet-printed polymer insulator induce the directional solvent evaporation and produce the formation of a bilateral ordered state of the TIPS-pentacene molecules, in contrast to the molecules radially oriented on the spin-coated insulator. The ordered molecular domains of TIPS-pentacene were examined by measuring the optical anisotropy and the mobility of the UT-dictated TIPS-pentacene film was found to increase by more than two compared to that of the isotropic case.

Lastly, a new type of the quasi-surface emissive VOLET with the help of a network source electrode of closed topology was constructed. Due to the closed topology, the charge transport and the carrier recombination processes

in 2-dimension, extended from a bilateral direction, were allowed. As a result, the light emission area was found to depend on the relative size of the aperture in the network electrode to the characteristic length scale for the charge carrier recombination. In this architecture, the luminance was well-controlled by the gate voltage through an organic semiconducting layer over the network source electrode.

In conclusion, the recent advances in the electrical performance of organic semiconductors have led to the advent of a new area of organic electronics including flexible and large-area electronics, low-cost printed electronics, and optoelectronics. Considering that organic electronic devices consist of multi-layers, generating a variety of interfaces involving complex physicochemical phenomena, further improvement of the device performance still remains to be achieved through engineering the interfaces or constructing the novel architectures besides tailoring the organic materials. Therefore, the approaches presented though this thesis are promising to play a primary role for the investigation of physical phenomena among different layers and the development of advanced electronic and/or optoelectronic applications.

Appendix (acronyms)

α-NPD: N,N'-di(1-naphthyl)-N,N'-diphenylbenzidine

Alq_3: tri-(8-hydroxyquinoline)aluminum

CNT: carbon nanotube

DI: deionized

DOD: drop-on-demand

EL: electroluminescence

FWHM: full width at half maximum

HOMO: highest occupied molecular orbitals

ITO: indium-tin-oxide

LUMO: lowest unoccupied molecular orbitals

MIM: metal-insulator-metal

MISM: metal-insulator-semiconductor-metal

MMF: methylated poly(melamine-co-formaldehyde)

OFET: organic field-effect transistor

OLED: organic light-emitting diode

OLET: organic light-emitting transistor

OPV: organic photovoltaic

OSC: organic semiconductor

PDB: patterned dielectric barrier

PDMS: poly(dimethylsioxane)

PEM: photoelastic modulator

PGMEA: propylene glycol methyl ether acetate

PR: photoresist

PVP: poly(4-vinylphenol)

RT: room temperature

SAM: self-assembled monolayer

TIPS: 6,13-bis(triisopropylsilylethynyl)

UT: unidirectional topography

VOFET: vertical organic field-effect transistor

VOLET: vertical organic light-emitting transistor

XRD: X-ray diffraction

Bibliography

[1] J. E. Anthony, J. S. Brooks, D. L. Eaton, and S. R. Parkin, *J. Am. Chem. Soc.* **123**, 9482 (2001).

[2] J. Zhang, J. Wang, H. B. Wang, and D. H. Yan, *Appl. Phys. Lett.* **84**, 142 (2004).

[3] M. H. Zhang, S. P. Tiwari, and B. Kippelen, *Org. Electron.* **10**, 1133 (2009).

[4] M. Muccini, *Nat. Mater.* **5**, 605 (2006).

[5] F. Cicoira and C. Santato, *Adv. Funct. Mater.* **17**, 3421 (2007).

[6] R. Capelli, S. Toffanin, G. Generali, H. Usta, A. Facchetti, and M. Muccini, *Nat. Mater.* **9**, 496 (2010).

[7] J. Liu, I. Engquist, X. Crispin, and M. Berggren, *J. Am. Chem. Soc.* **134**, 901 (2012).

[8] B. B. Y. Hsu, C. H. Duan, E. B. Namdas, A. Gutacker, J. D. Yuen, F. Huang, Y. Cao, G. C. Bazan, I. D. W. Samuel, and A. J. Heeger, *Adv. Mater.* **24**, 1171 (2012).

[9] H. S. Seo, D. K. Kim, J. D. Oh, E. S. Shin, and J. H. Choi, *J. Phys. Chem. C* **117**, 4764 (2013).

[10] J. Zaumseil, R. H. Friend, and H. Sirringhaus, *Nat. Mater.* **5**, 69 (2005).

[11] J. Zaumseil, C. L. Donley, J. S. Kim, R. H. Friend, and H. Sirringhaus, *Adv. Mater.* **18**, 2708 (2006).

[12] S. Toffanin, R. Capelli, W. Koopman, G. Generali, S. Cavallini, A. Stefani, D. Saguatti, G. Ruani, and M. Muccini, *Laser Photonics Rev.* **7**, 1011 (2013).

[13] P. Stallinga, *Electrical characterization of organic electronic materials and devices*. John Wiley & Sons, Ltd, Chichester, UK (2009).

[14] H. Klauk, *Organic Electronics II: More Materials and Applications*. Wiley-VCH, Weinheim, Germany (2012).

[15] Z. Bao and J. J. Locklin, *Organic field-effect transistors*. CRC Press, Boca Raton, USA (2007).

[16] F. Amy, C. Chan, and A. Kahn, *Org. Electron.* **6**, 85 (2005).

[17] S. Kobayashi, T. Nishikawa, T. Takenobu, S. Mori, T. Shimoda, T. Mitani, H. Shimotani, N. Yoshimoto, S. Ogawa, and Y. Iwasa, *Nat Mater* **3**, 317 (2004).

[18] S. J. Han, J. H. Kim, J. W. Kim, C. K. Min, S. H. Hong, D. H. Kim, K. H. Baek, G. H. Kim, L. M. Do, and Y. Park, *J. Appl. Phys.* **104**, 013715 (2008).

[19] C. S. Kim, S. J. Jo, J. B. Kim, S. Y. Ryu, J. H. Noh, H. K. Baik, S. J. Lee, and Y. S. Kim, *Appl. Phys. Lett.* **91**, 063503 (2007).

[20] M. H. Kim, S. P. Noh, C. M. Keum, J. H. Bae, and S. D. Lee, *Org. Electron.* **13**, 2365 (2012).

[21] H. Yan, Z. Chen, Y. Zheng, C. Newman, J. R. Quinn, F. Dotz, M. Kastler, and A. Facchetti, *Nature* **457**, 679 (2009).

[22] M. Mas-Torrent and C. Rovira, *Chem. Soc. Rev.* **37**, 827 (2008).

[23] S. Allard, M. Forster, B. Souharce, H. Thiem, and U. Scherf, *Angew. Chem. Int. Ed. Engl.* **47**, 4070 (2008).

[24] H. Sirringhaus, T. Kawase, R. H. Friend, T. Shimoda, M. Inbasekaran, W. Wu, and E. P. Woo, *Science* **290**, 2123 (2000).

[25] T. Sekitani, Y. Noguchi, U. Zschieschang, H. Klauk, and T. Someya, *Proc. Natl. Acad. Sci. USA* **105**, 4976 (2008).

[26] Y. H. Kim, B. Yoo, J. E. Anthony, and S. K. Park, *Adv. Mater.* **24**, 497 (2012).

[27] H. E. Katz, A. J. Lovinger, J. Johnson, C. Kloc, T. Siegrist, W. Li, Y. Y. Lin, and A. Dodabalapur, *Nature* **404**, 478 (2000).

[28] P. G. de Gennes, *Rev. Mod. Phys.* **57**, 827 (1985).

[29] R. N. Wenzel, *Ind. Eng. Chem.* **28**, 988 (1936).

[30] A. B. D. Cassie and S. Baxter, *Trans. Faraday Soc.* **40**, 0546 (1944).

[31] P.-G. d. Gennes, F. Brochard-Wyart, and D. Quéré, *Capillarity and wetting phenomena : drops, bubbles, pearls, waves*. Springer, New York, USA (2004).

[32] J. Z. Wang, Z. H. Zheng, H. W. Li, W. T. Huck, and H. Sirringhaus, *Nat. Mater.* **3**, 171 (2004).

[33] P. Calvert, *Chem. Mater.* **13**, 3299 (2001).

[34] T. N. Ng, S. Sambandan, R. Lujan, A. C. Arias, C. R. Newman, H. Yan, and A. Facchetti, *Appl. Phys. Lett.* **94**, 233307 (2009).

[35] S. Magdassi, *The chemistry of inkjet inks*. World Scientific, Hackensack, USA (2010).

[36] Y. Y. Noh, N. Zhao, M. Caironi, and H. Sirringhaus, *Nat Nanotechnol* **2**, 784 (2007).

[37] R. F. Pierret, *Semiconductor device fundamentals*. Addison-Wesley, Boston, USA (1996).

[38] G. Horowitz, P. Lang, M. Mottaghi, and H. Aubin, *Adv. Funct. Mater.* **14**, 1069 (2004).

[39] Z. Xu, S.-H. Li, L. Ma, G. Li, and Y. Yang, *Appl. Phys. Lett.* **91**, 092911 (2007).

[40] K. Nakamura, T. Hata, A. Yoshizawa, K. Obata, H. Endo, and K. Kudo, *Jpn. J. Appl. Phys.* **47**, 1889 (2008).

[41] M. A. McCarthy, B. Liu, E. P. Donoghue, I. Kravchenko, D. Y. Kim, F. So, and A. G. Rinzler, *Science* **332**, 570 (2011).

[42] L. Ma and Y. Yang, *Appl. Phys. Lett.* **85**, 5084 (2004).

[43] M. A. McCarthy, B. Liu, and A. G. Rinzler, *Nano Lett.* **10**, 3467 (2010).

[44] A. J. Ben-Sasson and N. Tessler, *Nano Lett.* **12**, 4729 (2012).

[45] H. Kleemann, A. A. Günther, K. Leo, and B. Lüssem, *Small* **9**, 3670 (2013).

[46] B. Liu, M. A. McCarthy, Y. Yoon, D. Y. Kim, Z. Wu, F. So, P. H. Holloway, J. R. Reynolds, J. Guo, and A. G. Rinzler, *Adv. Mater.* **20**, 3605 (2008).

[47] R. W. I. de Boer, N. N. Iosad, A. F. Stassen, T. M. Klapwijk, and A. F. Morpurgo, *Appl. Phys. Lett.* **86**, 032103 (2005).

[48] F. C. Chen, C. W. Chu, J. He, Y. Yang, and J. L. Lin, *Appl. Phys. Lett.* **85**, 3295 (2004).

[49] G. M. Wang, D. Moses, A. J. Heeger, H. M. Zhang, M. Narasimhan, and R. E. Demaray, *J. Appl. Phys.* **95**, 316 (2004).

[50] M. Egginger, M. Irimia-Vladu, R. Schwodiauer, A. Tanda, I. Frischauf, S. Bauer, and N. S. Sariciftci, *Adv. Mater.* **20**, 1018 (2008).

[51] J. M. Kim, J. W. Lee, J. K. Kim, B. K. Ju, J. S. Kim, Y. H. Lee, and M. H. Oh, *Appl. Phys. Lett.* **85**, 6368 (2004).

[52] Y. Jang, D. H. Kim, Y. D. Park, J. H. Cho, M. Hwang, and K. W. Cho, *Appl. Phys. Lett.* **88**, 072101 (2006).

[53] M. H. Yoon, H. Yan, A. Facchetti, and T. J. Marks, *J. Am. Chem. Soc.* **127**, 10388 (2005).

[54] D. K. Hwang, K. Lee, J. H. Kim, S. Im, C. S. Kim, H. K. Baik, J. H. Park, and E. Kim, *Appl. Phys. Lett.* **88**, 243513 (2006).

[55] H. Klauk, U. Zschieschang, J. Pflaum, and M. Halik, *Nature* **445**, 745 (2007).

[56] S. H. Ko, H. Pan, C. P. Grigoropoulos, C. K. Luscombe, J. M. J. Fréchet, and D. Poulikakos, *Nanotechnology* **18**, 345202 (2007).

[57] D. R. Hines, S. Mezhenny, M. Breban, E. D. Williams, V. W. Ballarotto, G. Esen, A. Southard, and M. S. Fuhrer, *Appl. Phys. Lett.* **86**, 163101 (2005).

[58] J.-F. Chang and H. Sirringhaus, *Adv. Mater.* **21**, 2530 (2009).

[59] H. S. Lee, D. Kwak, W. H. Lee, J. H. Cho, and K. Cho, *J. Phys. Chem. C* **114**, 2329 (2010).

[60] K.-J. Chang, F.-Y. Yang, C.-C. Liu, M.-Y. Hsu, T.-C. Liao, and H.-C. Cheng, *Org. Electron.* **10**, 815 (2009).

[61] S. C. B. Mannsfeld, A. Sharei, S. Liu, M. E. Roberts, I. McCulloch, M. Heeney, and Z. Bao, *Adv. Mater.* **20**, 4044 (2008).

[62] Z. Zheng, L. Yao, L. Xuan, and D. Shen, *Liquid Crystals* **38**, 17 (2011).

[63] S. H. Lee, M. H. Choi, S. H. Han, D. J. Choo, J. Jang, and S. K. Kwon, *Org. Electron.* **9**, 721 (2008).

[64] C.-M. Keum, J.-H. Bae, M.-H. Kim, W. Choi, and S.-D. Lee, *Org. Electron.* **13**, 778 (2012).

[65] W. Choi, M.-H. Kim, Y.-J. Na, and S.-D. Lee, *Org. Electron.* **11**, 2026 (2010).

[66] K. D. Kim and C. K. Song, *Appl. Phys. Lett.* **88**, 233508 (2006).

[67] S. C. Mannsfeld, M. L. Tang, and Z. Bao, *Adv. Mater.* **23**, 127 (2011).

[68] J. A. Lim, W. H. Lee, H. S. Lee, J. H. Lee, Y. D. Park, and K. Cho, *Adv. Funct. Mater.* **18**, 229 (2008).

[69] R. D. Deegan, *Phys. Rev. E* **61**, 475 (2000).

[70] C. W. Sele, B. K. C. Kjellander, B. Niesen, M. J. Thornton, J. B. P. H. van der Putten, K. Myny, H. J. Wondergem, A. Moser, R. Resel, A. J. J. M. van Breemen, N. van Aerle, P. Heremans, J. E. Anthony, and G. H. Gelinck, *Adv. Mater.* **21**, 4926 (2009).

[71] G. Giri, E. Verploegen, S. C. Mannsfeld, S. Atahan-Evrenk, H. Kim do, S. Y. Lee, H. A. Becerril, A. Aspuru-Guzik, M. F. Toney, and Z. Bao, *Nature* **480**, 504 (2011).

[72] R. L. Headrick, S. Wo, F. Sansoz, and J. E. Anthony, *Appl. Phys. Lett.* **92**, 063302 (2008).

[73] J. Park, C.-M. Keum, J.-H. Kim, S.-D. Lee, M. Payne, M. Petty, J. E. Anthony, and J.-H. Bae, *Appl. Phys. Lett.* **102**, 013306 (2013).

[74] A. L. Briseno, S. C. Mannsfeld, M. M. Ling, S. Liu, R. J. Tseng, C. Reese, M. E. Roberts, Y. Yang, F. Wudl, and Z. Bao, *Nature* **444**, 913 (2006).

[75] P. Liu, Y. Wu, Y. Li, B. S. Ong, and S. Zhu, *J. Am. Chem. Soc.* **128**, 4554 (2006).

[76] Z. R. He, K. Xiao, W. Durant, D. K. Hensley, J. E. Anthony, K. L. Hong, S. M. Kilbey, J. H. Chen, and D. W. Li, *Adv. Funct. Mater.* **21**, 3617 (2011).

[77] C.-M. Keum, J.-H. Bae, W.-H. Kim, M.-H. Kim, J. Park, and S.-D. Lee, *J. Korean Phys. Soc.* **58**, 1479 (2011).

[78] C. M. Keum, J. H. Kwon, S. D. Lee, and J. H. Bae, *Solid State Electron.* **89**, 189 (2013).

[79] F. Brochard, *Langmuir* **5**, 432 (1989).

[80] J.-H. Bae, J. Park, C.-M. Keum, W.-H. Kim, M.-H. Kim, S.-O. Kim, S. K. Kwon, and S.-D. Lee, *Org. Electron.* **11**, 784 (2010).

[81] D. H. Kim, D. Y. Lee, H. S. Lee, W. H. Lee, Y. H. Kim, J. I. Han, and K. Cho, *Adv. Mater.* **19**, 678 (2007).

[82] D. W. Berreman, *Phys. Rev. Lett.* **28**, 1683 (1972).

[83] R. D. Deegan, O. Bakajin, T. F. Dupont, G. Huber, S. R. Nagel, and T. A. Witten, *Nature* **389**, 827 (1997).

[84] H. Hu and R. G. Larson, *J. Phys. Chem. B* **110**, 7090 (2006).

[85] D. Soltman and V. Subramanian, *Langmuir* **24**, 2224 (2008).

[86] C. M. Keum, J. H. Bae, M. H. Kim, H. L. Park, M. M. Payne, J. E. Anthony, and S. D. Lee, *Appl. Phys. Lett.* **102**, (2013).

[87] M. Gleiche, L. F. Chi, and H. Fuchs, *Nature* **403**, 173 (2000).

[88] J. Y. Chung, J. P. Youngblood, and C. M. Stafford, *Soft Matter* **3**, 1163 (2007).

[89] W. Choi, A. Tuteja, J. M. Mabry, R. E. Cohen, and G. H. McKinley, *J. Colloid. Interf. Sci.* **339**, 208 (2009).

[90] S. G. Lee, H. S. Lim, D. Y. Lee, D. Kwak, and K. Cho, *Adv. Funct. Mater.* **23**, 547 (2013).

[91] A. Lafuma and D. Quere, *Nat. Mater.* **2**, 457 (2003).

[92] X. J. Feng and L. Jiang, *Adv. Mater.* **18**, 3063 (2006).

[93] J.-H. Kim, S. Kumar, and S.-D. Lee, *Phys. Rev. E* **57**, 5644 (1998).

[94] C.-J. Yu, J.-H. Bae, C.-M. Keum, and S.-D. Lee, *Curr. Appl. Phys.* **10**, 64 (2010).

[95] Y. L. Guo, G. Yu, and Y. Q. Liu, *Adv. Mater.* **22**, 4427 (2010).

[96] M. O'Neill and S. M. Kelly, *Adv. Mater.* **23**, 566 (2011).

[97] M. Muccini, W. Koopman, and S. Toffanin, *Laser Photonics Rev.* **6**, 258 (2012).

[98] A. Hepp, H. Heil, W. Weise, M. Ahles, R. Schmechel, and H. von Seggern, *Phys. Rev. Lett.* **91**, 157406 (2003).

[99] J. Zaumseil, R. H. Friend, and H. Sirringhaus, *Nat. Mater.* **5**, 69 (2006).

[100] E. B. Namdas, P. Ledochowitsch, J. D. Yuen, D. Moses, and A. J. Heeger, *Appl. Phys. Lett.* **92**, 183304 (2008).

[101] J. Zaumseil, C. R. McNeill, M. Bird, D. L. Smith, P. Paul Ruden, M. Roberts, M. J. McKiernan, R. H. Friend, and H. Sirringhaus, *J. Appl. Phys.* **103**, 064517 (2008).

[102] T. Oyamada, H. Sasabe, Y. Oku, N. Shimoji, and C. Adachi, *Appl. Phys. Lett.* **88**, 093514 (2006).

[103] K. Yamane, H. Yanagi, A. Sawamoto, and S. Hotta, *Appl. Phys. Lett.* **90**, 162108 (2007).

[104] M. Schidleja, C. Melzer, and H. von Seggern, *Appl. Phys. Lett.* **94**, 123307 (2009).

[105] N. Suganuma, N. Shimoji, Y. Oku, S. Okuyama, and K. Matsushige, *Org. Electron.* **9**, 834 (2008).

[106] V. Maiorano, A. Bramanti, S. Carallo, R. Cingolani, and G. Gigli, *Appl. Phys. Lett.* **96**, 133305 (2010).

[107] K. Nakamura, T. Hata, A. Yoshizawa, K. Obata, H. Endo, and K. Kudo, *Appl. Phys. Lett.* **89**, 103525 (2006).

[108] A. J. Ben-Sasson, Z. H. Chen, A. Facchetti, and N. Tessler, *Appl. Phys. Lett.* **100**, 263306 (2012).

[109] N. J. Watkins, L. Yan, and Y. Gao, *Appl. Phys. Lett.* **80**, 4384 (2002).

[110] S. K. So, W. K. Choi, L. M. Leung, and K. Neyts, *Appl. Phys. Lett.* **74**, 1939 (1999).

Publications

[1] International Journals

1. **C.-M. Keum**, I.-H. Lee, S.-H. Lee, G. J. Lee, M.-H. Kim, and S.-D. Lee, "Quasi-surface emission in vertical organic light-emitting transistors with network electrode", *Optics Express*, **22**, 14750 (2014).
2. I.-H. Lee, S.-H. Lee, **C.-M. Keum**, S.-U. Kim, and S.-D. Lee, "Combinatorial color arrays based on optical micro-resonators in monolithic architecture", *Optics Express*, **22**, 15320 (2014).
3. G. J. Lee, M.-H. Kim, S.-P. Noh, **C.-M. Keum**, and S.-D. Lee, "Ambipolar-type organic field-effect transistor with two stacked active layers in dual-gate configuration", *Molecular Crystals and Liquid Crystals*, Accepted for publication.
4. S. Kim, Y.-S. Ryu, J.-H. Suh, **C.-M. Keum**, Y. Sohn, S.-D. Lee, "Biocompatible patterning of proteins on wettability gradient surface by thermo-transfer printing", *Journal of Nanoscience and Nanotechnology*, **14**, 6069 (2014).
5. S. M. Cho, **C.-M. Keum**, H.-L. Park, M.-H. Kim, J.-H. Bae, and S.-D. Lee, "Integrated polymer solar cells in serial architecture with patterned charge-transporting MoO_x for miniature high-voltage sources", *Japanese Journal of Applied Physics*, **53**, 042301 (2014).

6. M.-H. Kim, G. J. Lee, **C.-M. Keum**, and S.-D. Lee, “Concept of rewritable organic ferroelectric random access memory in two lateral transistors-in-one cell architecture”, *Semiconductor Science and Technology*, **29**, 025004 (2014).

7. M.-H. Kim, **C.-M. Keum**, and S.-D. Lee, “Tailoring and patterning of dielectric interfaces for the development of advanced organic field-effect transistors”, *Liquid Crystals*, **41**, 310 (2014).

8. **C.-M. Keum**, J.-H. Kwon, S.-D. Lee, and J.-H. Bae, “Control of the molecular order and cracks of the 6,13-bis(triisopropylsilylethynyl)-pentacene on a polymeric insulator by anisotropic solvent drying”, *Solid-State Electronics*, **89**, 189 (2013).

9. **C.-M. Keum**, J.-H. Bae, M.-H. Kim, H.-L. Park, M. M. Payne, J. E. Anthony, and S.-D. Lee, “Topography-guided spreading and drying of 6,13-bis(triisopropylsilylethynyl)-pentacene solution on a polymer insulator for the field-effect mobility enhancement”, *Applied Physics Letters*, **102**, 193307 (2013).

10. M.-H. Kim, G. J. Lee, **C.-M. Keum**, and S.-D. Lee, “Voltage-readable nonvolatile memory cell with programmable ferroelectric multistates in organic inverter configuration”, *Organic Electronics*, **14**, 1231 (2013).

11. J. Park, **C.-M. Keum**, J.-H. Kim, S.-D. Lee, M. Payne, M. Petty, J. E. Anthony, and J.-H. Bae, “Photo-assisted molecular engineering for high anisotropic mobility in a blended organic semiconductor used transistor with a polymeric insulator”, *Applied Physics Letters*, **102**, 013306 (2013).

12. M.-H. Kim, S.-P. Noh, **C.-M. Keum**, J.-H. Bae, S.-D. Lee, “Control of interfacial charges of organic semiconductor by transverse dipolar field for high noise-margin inverters with full-swing capability”, *Organic Electronics*, **13**, 2365 (2012).

13. M.-H. Kim, S.-P. Noh, **C.-M. Keum**, and S.-D. Lee, “Bias voltage effect on electrical properties of N-type polymeric field effect transistors with dual gate electrodes”, *Molecular Crystals and Liquid Crystals*, **567**, 34 (2012).

14. **C.-M. Keum**, J.-H. Bae, M.-H. Kim, W. Choi, S.-D. Lee, “Solution-processed low leakage organic field-effect transistors with self-pattern registration based on patterned dielectric barrier”, *Organic Electronics*, **13**, 778 (2012).

15. **C.-M. Keum**, J.-H. Bae, W.-H. Kim, M.-H. Kim, and S.-D. Lee, “Effect of thermo-gradient assisted solvent evaporation on enhancement of electrical properties of 6,13-bis(triisopropylsilylethynyl)-pentacene thin-film transistors”, *Journal of the Korean Physical Society*, **58**, 1479 (2011).

16. M.-H. Kim, J.-H. Bae, W.-H. Kim, **C.-M. Keum**, and S.-D. Lee, “Chevron-type gate configuration of short channel top-contact organic thin-film transistors using a polymeric tilt support”, *Journal of Physics D: Applied Physics*, **44**, 145106 (2011).

17. W.-H. Kim, J.-H. Bae, M.-H. Kim, **C.-M. Keum**, and S.-D. Lee, “Surface modification of a ferroelectric polymer insulator for low-voltage readable

nonvolatile memory in an organic field-effect transistor", *Journal of Applied Physics*, **109**, 024508 (2011).

18. J. Park, J.-H. Bae, W.-H. Kim, M.-H. Kim, **C.-M. Keum**, S.-D. Lee, and J. S. Choi, "Effects of interfacial charge depletion in organic thin-film transistors with polymeric dielectrics on electrical stability", *Materials*, **3**, 3614 (2010).
19. J.-H. Bae, J. Park, **C.-M. Keum**, W.-H. Kim, M.-H. Kim, S.-O. Kim, S. K. Kwon, and S.-D. Lee, "Thermal annealing effect on the crack development and the stability of 6,13-bis(triisopropylsilyl ethynyl)-pentacene field-effect transistors with a solution-processed polymer insulator", *Organic Electronics*, **11**, 784 (2010).
20. C.-J. Yu, J.-H. Bae, **C.-M. Keum**, and S.-D. Lee, "Optical anisotropy of aligned pentacene molecules on a rubbed polymer corresponding to the electrical anisotropy", *Current Applied Physics*, **10**, 64 (2010).

[2] International Conferences

1. G. Lee, **C.-M. Keum**, M.-H. Kim, and S.-D. Lee, "Mobility enhancement in 6,13-bis(triisopropylsilylethynyl)-pentacene based field-effect-transistor with semiconducting organic buffer layer", *10th International Conference on Organic Electronics* (Modena, Italy), (2014)

2. H.-L. Park, **C.-M. Keum**, B.-Y. Lee, S.-H. Lee, and S.-D. Lee, “Engineering the work function of inkjet-printed electrodes in all-solution-processed organic field-effect transistors”, *European Materials Research Society Spring Meeting* (Lille, France), DD-9, (2014).

3. H.-L. Park, S.-H. Lee, **C.-M. Keum**, I.-H. Lee, and S.-D. Lee, “Effect of surface wettability and topography of an insulator on mobility enhancement of soluble organic semiconductors”, *European Materials Research Society Spring Meeting* (Lille, France), DD-15, (2014).

4. M. Bortnichenko, G. J. Lee, **C.-M. Keum**, S.-H. Lee, E.-S. Yu, and Sin-Doo Lee, “Effect of oxygen plasma treatment of Ag electrode on mobility enhancement in organic thin-film transistors”, *25th International Conference on Molecular Electronics & Devices* (Seoul, Korea), (2014).

5. **C.-M. Keum**, I.-H. Lee, G.-J. Lee, H.-L. Park, S.-H. Lee, and S.-D. Lee, “Quasi-surface emissive vertical organic light-emitting field-effect transistors with network source electrode”, *Materials Research Society Spring Meeting* (San Francisco, USA), p. 300 (2014).

6. I.-H. Lee, S.-H. Lee, **C.-M. Keum**, and S.-D. Lee, “Patterned structural color based on multilevel optical microcavity by microcontact printing”, *Materials Research Society Spring Meeting* (San Francisco, USA), p. 317 (2014).

7. **C.-M. Keum**, S.-M. Cho, G.-J. Lee, H.-L. Park, M.-H. Kim, and S.-D. Lee, “Importance of patterning a charge transport layer of MoO_x for the high open circuit voltage in integrated polymer solar cells”, *9th*

International Conference on Organic Electronics (Grenoble, France), PC81. (2013)

8. G.-J. Lee, S.-P. Noh, M.-H. Kim, C.-M. Keum, and S.-D. Lee, “Ambipolar organic field-effect transistors by two stacked unipolar organic semiconducting layers in a dual-gate configuration”, *9th International Conference on Organic Electronics* (Grenoble, France), PC127 (2013).

9. M.-H. Kim, **C.-M. Keum**, G. J. Lee, and S.-D. Lee, “Lateral integration of ferroelectric and paraelectric organic field-effect transistors for unipolar organic inverter with high noise-margin”, *International Conference on Electronic Materials and Nanotechnology for Green Environment* (Jeju, Korea), (2012).

10. **C.-M. Keum**, M.-H. Kim, H.-L. Park, and S.-D. Lee, “Effect of microstructures of an ink-jet printed polymer insulator on the molecular ordering of 6,13-bis(triisopropylsilylethynyl)-pentacene”, *International Conference on Electronic Materials and Nanotechnology for Green Environment* (Jeju, Korea), (2012).

11. **C.-M. Keum**, H.-L. Park, and S.-D. Lee, “Charge injection in solution-processed field-effect transistor controlled by asymmetric work functions of ink-jet printed electrodes”, *8th International Conference on Organic Electronics* (Tarragona, Spain), P2.11 (2012).

12. **C.-M. Keum**, M.-H. Kim, J. Shim, Y.-J. Na, I. Kymissis, and S.-D. Lee, “Spreading and drying mechanism for inkjet printing of high-resolution

patterns embedded in flexible substrates", *Large-area, Organic & Printed Electronics - Convention* (Munich, Germany), p. 335 (2012).

13. M.-H. Kim, G. J. Lee, **C.-M. Keum**, I.-H. Lee, and S.-D. Lee, "Integration of ferroelectric and paraelectric organic field-effect transistors by transfer-printing of a dielectrically screening layer for ferroelectric random-access-memory", *European Materials Research Society Spring Meeting* (Strasbourg, France), H-20 (2012).

14. M.-H. Kim, G. J. Lee, **C.-M. Keum**, and S.-D. Lee, "Fabrication of ferroelectric random-access-memory cell with two switching- and ferroelectric organic field-effect transistors using transfer-printed buffer layer", *Materials Research Society Spring Meeting* (San Francisco, USA), p. 150 (2012).

15. W. Choi, M.-H. Kim, **C.-M. Keum**, and S.-D. Lee, "Sacrificial layer-assisted fabrication of high-resolution light-emitting diodes", *International Photonics Conference*, (Tainan, Taiwan) (2011).

16. M.-H. Kim, S.-P. Noh, **C.-M. Keum**, W. Choi, and S.-D. Lee, "Fabrication of the enhanced and depletion mode organic transistors for full-swing inverters using different polymers", *Materials Research Society Spring Meeting* (San Francisco, USA), p. 200 (2011).

17. **C.-M. Keum**, M.-H. Kim, and S.-D. Lee, "Charge transport enhancement in TIPS-pentacene by formation of micro-structured PVP insulator using ink-jet printing", *Materials Research Society Spring Meeting* (San Francisco, USA), p. 200 (2011).

18. **C.-M. Keum**, J.-H. Bae, W. Choi, W.-H. Kim, M.-H. Kim, and S.-D. Lee, "Leakage reduction in 6,13-bis(triisopropylsilylethynyl)-pentacene based organic thin-film transistors with patterned dual gate insulator", *International Conference on Electronic Materials and Nanotechnology for Green Environment* (Jeju, Korea), p. 44 (2010).

19. **C.-M. Keum**, J.-H. Bae, S.-M. Cho, and S.-D. Lee, "Deposition rate dependence of the initial layer growth of pentacene on a topologically modified polymeric insulator", *7th International Conference on Organic Electronics* (Paris, France), p. 71 (2010).

20. S.-M. Cho, **C.-M. Keum**, E. Jang, and S.-D. Lee, "Importance of the fibrillar morphology for the device performances of a polymer photovoltaic device with a diffusive heterojunction structure", *7th International Conference on Organic Electronics* (Paris, France), p. 118 (2010).

21. W.-H. Kim, J.-H. Bae, M.-H. Kim, **C.-M. Keum**, and S.-D. Lee, "Double polymer layer for a high dielectric gate insulator in 6,13-bis(triisopropylsilylethynyl)-pentacene field-effect transistor", *10th International Meeting on Information Display* (Seoul, Korea), p. 13 (2010).

22. W. Choi, M.-H. Kim, **C.-M. Keum**, and S.-D. Lee, "Application of transfer-printed hydrophobic layer for high-resolution organic electronic devices with solution-processed polymers", *Materials Research Society Spring Meeting* (San Francisco, USA), p. 98 (2010).

23. J.-H Na, **C.-M. Keum**, Y.-J. Na, and S.-D. Lee, “A ferroelectric liquid crystal display with low operation voltage in a pixel-confined geometry”, *International Display Workshop* (Miyazaki, Japan), p. 111 (2009).

24. W.-H. Kim, J.-H. Bae, M.-H. Kim, **C.-M. Keum**, and S.-D. Lee, “Effect of the UV ozone treatment on the threshold voltage shift in a ferroelectric field-effect-transistor”, *6th International Conference on Organic Electronics* (Liverpool, United Kingdom), p. 16 (2009).

25. J.-H. Bae, W.-H. Kim, M.-H. Kim, **C.-M. Keum**, J. S. Choi, and S.-D. Lee, “Relationship between the magnitude of the leakage current and the size of the grain boundary in a pentacene transistor”, *6th International Conference on Organic Electronics* (Liverpool, United Kingdom), p. 17. (2009).

26. M.-H. Kim, J.-H. Bae, W.-H. Kim, **C.-M. Keum**, and S.-D. Lee, “Fabrication of trapezoid-shaped organic thin film transistors for large driving drain current”, *Materials Research Society Spring Meeting* (San Francisco, USA), p. 90 (2009).

27. J.-H. Bae, W.-H. Kim, M.-H. Kim, **C.-M. Keum**, and S.-D. Lee, “Interfacial effects of polymeric gate insulators on device performances of organic thin-film transistors”, *214th Meeting of ECS Prime* (Hawii, USA), p. 1860 (2008).

28. J.-H. Bae, W.-H. Kim, M.-H. Kim, **C.-M. Keum**, J. S. Choi, and S.-D. Lee, “Physical origin of the leakage current in an organic thin-film

transistor with a high dielectric nanocomposite layer", *20th Korea Japan Joint Forum* (Hokkaido, Japan), p. 25-088 (2008).

29. J.-H. Bae, **C.-M. Keum**, S.-D. Lee, and C.-J Yu, "Optical anisotropy of aligned pentacene molecules on a rubbed polymer", *20th Korea Japan Joint Forum*, Hokkaido, Japan, p. 25-089 (2008).

[3] Domestic Conferences

1. **C.-M. Keum**, J.-H. Bae, W.-H. Kim, M.-H. Kim, J Park, and S.-D. Lee, "Mobility enhancement in solution-processed organic thin-film transistor using gradual temperature curing method", *17th Korean Conference on Semiconductors* (Daegu, Korea), p. 604 (2010).

2. J. Park, J.-H. Bae, W.-H. Kim, M.-H. Kim, **C.-M. Keum**, and S.-D. Lee, "Influence of surface properties of gate insulator on pentacene growth and organic field-effect transistor characteristics", *17th Korean Conference on Semiconductors* (Daegu, Korea), p. 602 (2010).

3. W.-H. Kim, M.-H. Kim, J.-H. Bae, **C.-M. Keum**, and S.-D. Lee, "Mobility enhancement in a ferroelectric field-effect transistor with a ferroelectric polymer insulator by CF4 plasma treatment", *16th Korean Conference on Semiconductors* (Daegu, Korea), p. 772 (2009).

Abstract (Korean)

최근 유기 재료 및 유기 소자의 전기적 성능과 그에 대한 물리적 이해가 발전함에 따라 대면적의 유연성 전자 공학, 저가격 인쇄 전자, 광전자공학 등을 포함하는 유기 전자 공학의 시대가 도래하고 있다. 유기 반도체 물질은 본질적으로 합성이 용이하며 다양한 공정이 가능하기 때문에 넓은 범위의 방법을 통해 기능성 물질을 제조하고 유기 전자 소자를 제작할 수 있다는 장점이 있다. 대표적인 유기 전자 소자 중 하나인 유기 전계 효과 트랜지스터는 플렉서블 디스플레이(flexible display), 전파 인식 태그, 센서 등과 같은 실제 응용 기술의 핵심 요소가 될 것으로 여겨지고 있다.

유기 전계 효과 트랜지스터와 관련된 많은 쟁점 중, 여러 가지 용액 공정 방법은 저온에서 공정이 가능할 뿐만 아니라 롤투롤(roll-to-roll) 공정이나 잉크젯 프린팅(inkjet printing) 등의 인쇄 공정처럼 간단하다는 점에서, 유연성을 지닌 대면적의 저가격 유기 전자 소자의 제작 방법으로 각광받고 있다. 용액 공정은 기본적으로 고체 표면 상에서 액체가 퍼지고 마르는 과정을 수반하기 때문에, 고체/액체 사이의 계면 조절 및 액체의 열역학적 거동에 대한 이해가 반드시 필요하다.

한편, 복잡한 전자공학, 광전자공학적 시스템(system)을 구현하기 위해 유기 전계 효과 트랜지스터의 기능적인 측면이

강조되고 있다. 예를 들어, 트랜지스터의 전기적 스위칭(switching) 성질과 발광 소자로서의 특성을 동시에 지니고 있는 유기 발광 트랜지스터는 향후 차세대 디스플레이 기술로서 큰 잠재력을 가지고 있다. 이러한 유기 발광 트랜지스터는 양자효율이나 개구율 측면에서 유기 발광 다이오드를 넘어서는 장점을 보이지만, 전형적인 소자 구조에서는 본질적인 선발광 특성으로 인해 일부 응용 기술로만 적용될 수 있다는 한계가 있다.

본 논문은 고성능 유기 전계 효과 트랜지스터 및 유기 발광 트랜지스터를 개발하기 위한 기능층의 단계적 공정 기술들을 제시하며, 용액 공정 유기 전계 효과 트랜지스터 및 준면발광 유기 발광 트랜지스터에 초점을 맞춰서 크게 두 부분으로 나뉘어진다.

우선, 용액 공정 유기 전계 효과 트랜지스터에 장벽 모양의 패턴이 형성된 유전체 구조를 도입하여 누설전류를 줄이고 다층 구조의 자동 정렬을 유도하는 기술을 제안한다. 소수성의 불소계 고분자로 이루어진 이 유전체 구조는 게이트 전극으로부터 발생하는 수직 방향의 전하 흐름을 효과적으로 차단함과 동시에 선택적 젖음 현상과 기하학적 구조물을 통해 활성층 패턴을 자동으로 형성하는 역할을 한다. 다음으로, 용액 공정 유기 반도체의 분자 정렬을 유도하고 결과적으로 전하 이동도를 향상시킬 수 있는 두 가지 기술을 도입한다. 용액 공정 유기 반도체 물질의 분자 정렬은 용액이 퍼지고 마르는 과정에 영향을 받기

때문에, 이 과정을 제어함으로써 용액 공정 기반의 유기 전자 소자의 전기적 특성을 조절할 수 있다. 온도구배를 통한 비등방적 용매 증발 방식을 적용하거나 잉크젯 프린팅으로 형성된 단방향의 표면 구조를 갖는 고분자 절연막을 이용한 방식을 도입하여 용액 공정 시 용매가 퍼지고 마르는 과정을 조절한다.

두 번째로, 그물 형태의 네트워크(network) 전극을 개발하여 준면발광 특성을 갖는 수직 유기 발광 트랜지스터를 구현한다. 네트워크 소스(source) 전극 내의 폐쇄된 공간 구조로 인해, 전하 이동 및 그에 따른 전하 재결합은 네트워크 경계에서 각각 공간의 중심 방향으로 확대된다. 이는 면발광의 공간적 분포는 전하 재결합의 특성 길이에 대한 네트워크 전극 내의 공간의 상대적인 크기에 의존한다는 것을 의미한다. 또한 전하 재결합을 통해 발광이 일어나는 영역을 거시적인 수준에서 관찰하기 위한 광학적 방법을 새롭게 개발한다.

요약하면, 여러 가지 기능층 사이에 일어나는 계면 현상의 관점에서 고성능 유기 전자 및 광전자소자의 개발을 위한 기능층의 단계적 공정 및 새로운 소자 구조를 연구한다. 본 논문에서 제시된 연구는 용액 공정 유기 전자 소자의 계면에서 형성되는 다양한 유기 물질의 조직을 제어하고 다층구조에서의 계면을 조절하며 유기 전자 소자의 기본 구성 요소를 집적하는 데 있어 중요한 길을 제시할 것으로 기대된다.

주요어: 유기전계효과트랜지스터, 유기발광트랜지스터, 용액공정, 잉크젯 프린팅, 소자 구조, 네트워크 전극

학번: 2008-20827